nature communications

Article

https://doi.org/10.1038/s41467-024-54413-9

Width-dependent continuous growth of atomically thin quantum nanoribbons from nanoalloy seeds in chalcogen vapor

Received: 20 May 2024

Accepted: 10 November 2024

Published online: 21 November 2024

Check for updates

Xufan Li[1,11], Samuel Wyss[2,11], Emanuil Yanev[3,11], Qing-Jie Li[4,5], Shuang Wu[1], Yongwen Sun[6,7], Raymond R. Unocic[8,9], Joseph Stage[2], Matthew Strasbourg[2], Lucas M. Sassi[1,10], Yingxin Zhu[6,7], Ju Li[4,5], Yang Yang[6,7], James Hone[3], Nicholas Borys[2], P. James Schuck[3] & Avetik R. Harutyunyan[1]

Nanoribbons (NRs) of atomic layer transition metal dichalcogenides (TMDs) can boost the rapidly emerging field of quantum materials owing to their width-dependent phases and electronic properties. However, the controllable downscaling of width by direct growth and the underlying mechanism remain elusive. Here, we demonstrate the vapor-liquid-solid growth of single crystal of single layer NRs of a series of TMDs (MeX_2: Me = Mo, W; X = S, Se) under chalcogen vapor atmosphere, seeded by pre-deposited and respective transition metal-alloyed nanoparticles that also control the NR width. We find linear dependence of growth rate on supersaturation, known as a criterion for continues growth mechanism, which decreases with decreasing of NR width driven by the Gibbs-Thomson effect. The NRs show width-dependent photoluminescence and strain-induced quantum emission signatures with up to ≈ 90% purity of single photons. We propose the path and underlying mechanism for width-controllable growth of TMD NRs for applications in quantum optoelectronics.

One-dimensional (1D) or quasi-1D electronic systems including whiskers, nanowires, and nanotubes exhibit exotic physical properties[1–5], which continue to fuel fundamental research and advanced applications. Recently, quasi-1D structures such as graphene nanoribbons (NRs) have been synthesized[6–10], showing enriched electronic structures and quantum phase tuning[6–9] compared to graphene sheets. Theoretical calculations also predicted width-dependent crystalline phases, band structure, and spin-orbit coupling in NRs of atomically thin two-dimensional (2D) transition metal dichalcogenides (TMDs)[11–15]. These anticipated peculiarities have attracted broad interest in creating disruptive technologies, especially in the rapidly emerging area of 1D van der Waals (vdW) quantum materials[16]. To date, the dominant approach for obtaining TMD NRs with controllable widths relies on post-synthesis treatments (e.g., lithography or etching)[17–19]. There are also reports on NR growth mediated by liquid droplets of precursors[20,21], or guided growth on specifically engineered

[1]Honda Research Institute USA, Inc., San Jose, CA 95134, USA. [2]Department of Physics, Montana State University, Bozeman, MT 59717, USA. [3]Mechanical Engineering Department, Columbia University, New York, NY 10025, USA. [4]Department of Nuclear Science and Engineering, Massachusetts Institute of Technology, Cambridge, MA 02139, USA. [5]Department of Materials Science and Engineering, Massachusetts Institute of Technology, Cambridge, MA 02139, USA. [6]Department of Engineering Science and Mechanics, The Pennsylvania State University, University Park, PA 16802, USA. [7]Materials Research Institute, The Pennsylvania State University, University Park, PA 16802, USA. [8]Center for Nanophase Materials Sciences, Oak Ridge National Laboratory, Oak Ridge, TN 37831, USA. [9]Present address: Department of Materials Science and Engineering, North Carolina State University, Raleigh, NC 27695, USA. [10]Present address: Department of Physics, National University of Singapore, Singapore 117551, Singapore. [11]These authors contributed equally: Xufan Li, Samuel Wyss, Emanuil Yanev. e-mail: aharutyunyan@honda-ri.com

substrates through aligned steps[22–24] or chemical treatment[25] to realize aligned NRs with even controllable edge structures[24]. However, the results widths were generally >50 nm and still lack of control on the width. Recently, we reported a direct synthesis of bilayer MoS_2 NRs with width down to sub-10 nm after a mild treatment[18]. Nevertheless, interference with intrinsic properties by post-synthesis treatments and lack of effective control on NRs width during growth made it difficult to study their pristine width-confined properties, thereby hindering their potential applications. On the other hand, deeper understanding of NR growth mechanism could not only guide the direct width-controlled growth but also enrich the fundamental science as an example of formation of 1D or quasi-1D nanocrystals.

Among various established methods, chemical vapor deposition (CVD) has been widely used to synthesize various 1D or quasi-1D nanostructures in a broad diameter range[26–28], from which many peculiarities of growth mechanisms have been revealed since its first exploitation in the 1960s in the growth of Si whiskers[29–35]. Indeed, through classical analysis on the experimental finding that narrower whiskers grew more slowly, Givargizov[30] derived an empirical model predicting quadratic growth rate dependence on reciprocal of the diameter of Au-catalyzed Si whiskers with a critical diameter (≤50 nm), below which the whisker cannot grow. This diameter-dependence and limit was explained by Gibbs-Thomson effect, i.e., the supersaturation of silicon in Au–Si droplet decreases with the droplet size. However, although such a model was later confirmed by many studies on the growth of other semiconducting nanowires[29,33], there were reports showing diameter-independent growth rate, explained by irreversible catalytic dissociation of exploited Si precursor[34]. Moreover, there also have been reports showing the opposite growth rate-diameter relation where narrower nanowires grew faster due to adatom diffusion on the nanowire surface[31,32]. However, the growth mechanism of atomically thin 1D NRs has barely been studied.

In this work, we present a CVD growth of single layer (SL) TMD NRs mediated by seed nanoparticles (NPs) in chalcogen vapor atmosphere. The seed NPs are based on nanoalloys of metal precursor and catalyst (i.e., Mo-Ni or W-Mg), which also control the width of the grown NR. Based on the length vs. width analysis of grown SL MoS_2 NRs under different vapor supersaturation, we discover that unlike previously studied 1-D structures, i.e., whiskers and nanowires, the growth rate of NRs is a linear function of supersaturation, decreasing linearly with the reciprocal of width controlled by the Gibbs-Thomson effect, which is characteristic of continues growth. As an example of exploiting the quantum nature of the NRs, we demonstrate deterministic quantum emission (QE) signatures induced by localized strain, making them promising candidates as single photon sources for quantum communications.

Results

Growth of Single Layer MoS_2 NRs

Synthetic fluorophlogopite mica (F-mica) with (001) surface plane was used as the substrate, which has been used for vdW epitaxial growth of 2D flakes before[36]. Unlike typical one-step synthesis[18,20,21,37], we used a two-step growth approach: First formation of partial precursor/seed NPs followed by introduction of corresponding chalcogen vapor. Specifically taking MoS_2 as an example, we first deposited NPs on the substrate by evaporating a mixture of MoO_2, Ni, and NaBr powder under a moisturized Ar flow in a tube furnace system (Fig. 1a, step 1; Fig. 1b). The presence of NaBr enabled co-deposition of Ni and MoO_2. The deposited NPs are composed of Na-Mo-Ni-O (Fig. 2a, b), in which the Mo atomic ratio within (Mo-Ni) varies in a broad range of ≈10%-85%. It is important to note that the presence of moisture was essential for the formation of the Na-Mo-Ni-O compound from the precursor powder mixture; without moisture, only NaBr was deposited on the substrate (Supplementary Fig. 1a–c)[18]. The NPs were then exposed in a sulfur vapor atmosphere, generated by heating sulfur powder, in a separate tube reactor (Fig. 1a, step 2), resulting in "tip"-growth of MoS_2 NRs from the NPs, with widths comparable to the tip-NP (inset of Fig. 1c, Supplementary Fig. 2a, b) and lengths from a few to tens of micrometers (Fig. 1c, Supplementary Fig. 1). Despite the reduction of seed NPs' diameter during the NR growth (Supplementary Fig. 3), their diameter distribution correlates with that of NR width (Supplementary Fig. 2c), which allows control of width distribution of NRs through controlling the diameter distribution of pre-deposited seed NPs. It is also noted that in some areas the as-grown NRs show a certain extent of alignment (i.e., Fig. 1c) while in others they do not, which could be related to the specific surface condition and crystallographic orientations of the F-mica substrate.

Atomic force microscopy (AFM) analysis (Fig. 1d, Supplementary Fig. 2e) and Raman spectroscopy (Fig. 1e, Supplementary Fig. 4) confirm the SL MoS_2 NRs. Scanning transmission electron microscopy (STEM) with fast Fourier transform (FFT) analysis indicates that the NR is single crystal, with the axial growth along the [010] direction (Fig. 1f). Occasionally single crystal NR grown along the [110] direction was also observed (Supplementary Fig. 5). Atomic-resolution high-angle annular dark-field STEM (HAADF-STEM) shows clean, well-defined honeycomb lattice with a lattice parameter $a \approx 0.308$ nm of MoS_2 NRs, which is terminated by zigzag edge structures (Fig. 1g, Supplementary Fig. 5d, e). Detailed Auger electron spectroscopy (AES) analysis (Fig. 2a–c, Supplementary Fig. 6) and HAADF-STEM combined with FFT analysis (Fig. 2d–g) reveal that during NR growth the composition of seed NP evolved from Na-Mo-Ni-O (Fig. 2a, b) to a pure Ni NP with a face-centered cubic (fcc) structure (Fig. 2e, f), as a result of consumption of Mo atoms in the seed NP by MoS_2 NR through precipitation under S vapor atmosphere. The precipitation in turn drives the motion of NP along the axial growth direction of NR (see Supplementary Fig. 7 showing no motion of NP without precipitation). As the growth temperature in step 2 is above the liquefaction temperature of the seed NP (≈725 °C)[18], the growth follows a VLS mechanism. It should also be noted that Na and Ni were not detected from the NR in AES measurement (Fig. 2c, Supplementary Fig. 6), indicating that the as-grown NRs are purely MoS_2. The electrical properties of the SL MoS_2 NR at room temperature show typical n-type behavior with an on/off ratio of $\approx 10^6$ (Supplementary Fig. 8) and a current density comparable to the best CVD-grown MoS_2 reported with various contacts[38,39].

Growth mechanism of MoS_2 NRs

To understand the S-driven precipitation of MoS_2 on the atomic level and the role of multiple constituents in the seed NP, we performed molecular dynamics (MD) simulation (Fig. 2h). For an initially equilibrated Na-Mo-Ni-O NP at 650 K with S atoms, shows formation of triangular Mo-S local structural motifs bonded by Ni atoms, which could be the basic building blocks of MoS_2 NRs (Fig. 2i). Ni atoms also play a role in connecting different triangular units together (Fig. 2j). Those Mo-S motifs form even larger two-dimensional Mo-S structures as S continues to react with the system (Fig. 2k). It is noted that the oxygen in the system also plays an important role for the separation of Ni-MoS_2. In contrast to the equilibrated Na-Mo-Ni-O system with a relatively uniform distribution of all constituting elements (Supplementary Fig. 9b), the system without O (Na-Mo-Ni) evolves to a core-shell structure with Na atoms on the surface and a mixture of Ni and Mo in the interior of the nanoparticle (Supplementary Fig. 9c). Such a system keeps a core-shell structure after equilibrated with S atoms, only with slight mixing of Ni atoms with surface Na atoms (Supplementary Fig. 9a).

Next, we studied seed NP-mediated growth mechanism of SL MoS_2 NRs. As mentioned above, investigation on the relation of length (L) vs. diameter (d) of catalytic NP could provide specific insights on VLS growth mechanism of various 1D nanostructures. Therefore, we carefully analyzed our NR L vs. width (W) relationship grown at the same temperature ($T = 730$ °C) for a fixed growth duration $t = 180$ s.

https://doi.org/10.1038/s41467-024-54413-9

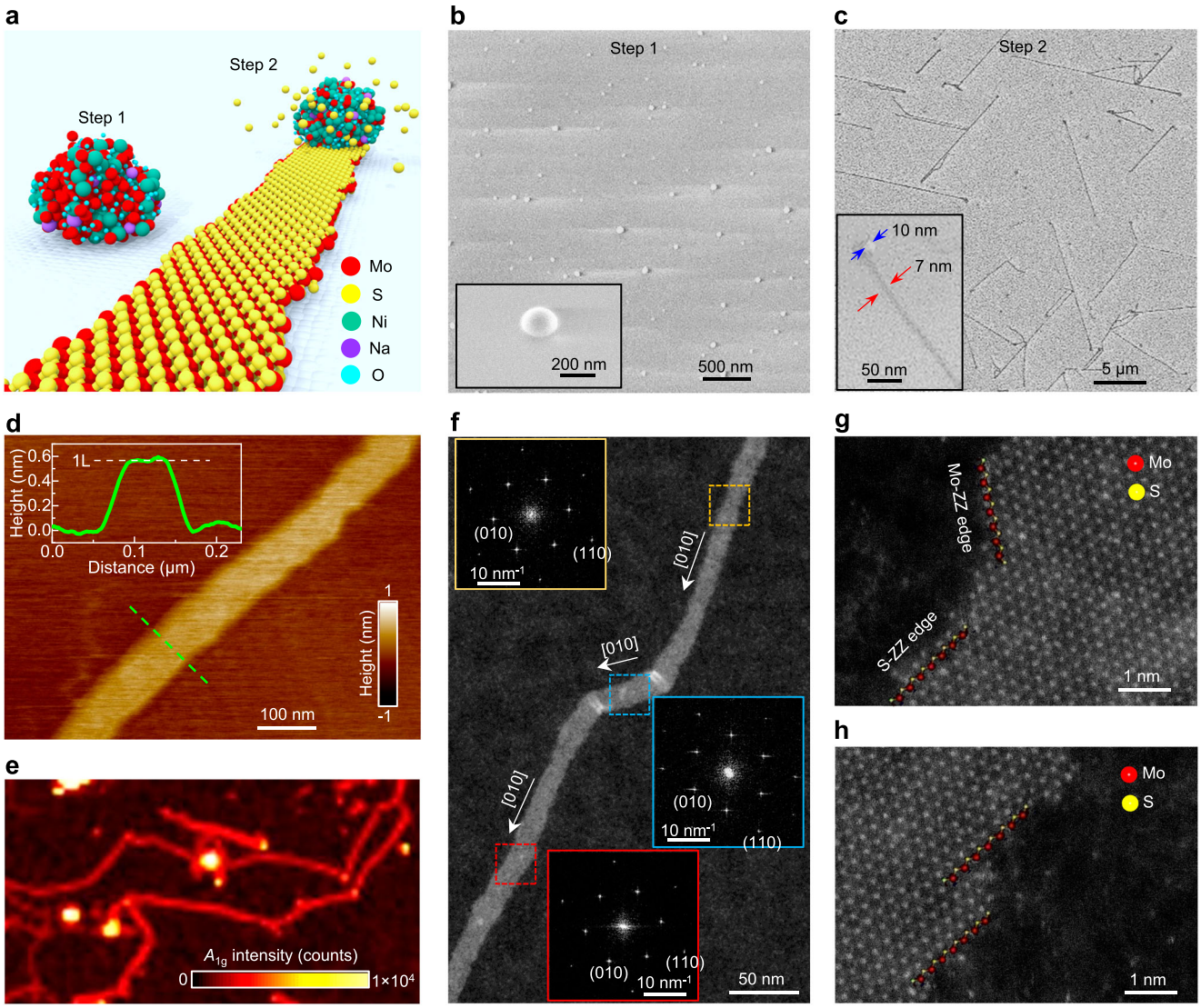

Fig. 1 | SL MoS_2 NRs grown on F-mica substrate. a Illustration of the two-step growth of SL MoS_2 NRs on F-mica substrate. Step 1: Seed NPs deposition. Step 2: Sulfurization of seed NPs resulting in precipitation of MoS_2 NR. Color code of the atoms: Mo (red), S (yellow), Ni (green), Na (purple), O (blue). **b** SEM image of Na-Mo-Ni-O seed NPs deposited for 1 min. Inset is the enlarged view of a NP. **c** SEM image of resulting MoS_2 NRs. Inset is the enlarged view of a NR width of ≈ 7 nm, comparable to the diameter of the tip Ni NP. **d** AFM image and height profile confirming the SL NR. **e** Raman intensity mapping of the A_{1g} peak of the SL MoS_2 NRs grown on F-mica. The color scales in (**d**, **e**) are linear. **f** Low-magnification HAADF-STEM image showing a length of ≈ 500 nm of a SL MoS_2 NR with two kinks. Insets with yellow, blue, and red borderlines are FFT patterns acquired from three different regions indicated by the dashed yellow, blue, and red boxes, respectively, indicating the growth axis of NR along the [010] crystal direction. The good alignment between the NR and diffraction pattern orientation, even in the kinked region (blue box), indicates the NR is single crystal. The kinks are used for strain analyses shown in Supplementary Fig. 19. **g**, **h** Atomic-resolution HAADF-STEM images showing edge structures of the upper side of the NR in the yellow box and lower side in red box, respectively, in (**f**). Although the FFT patterns and atomic resolution lattice show the edge is along the (110) plane, i.e., armchair, they are mostly terminated by zigzag structures resulting in steps. Source data are provided as a Source Data file.

Statistics on measured L and W of individual NRs grown under different sulfur vapor pressures (P_{sulfur}) (Supplementary Fig. 10) based on the SEM images (typical results shown in Supplementary Fig. 11) show a general trend that wider NRs grow longer than shorter ones (Fig. 3a). Since the NRs in general kept growing for $t > 180$ s (Supplementary Fig. 12), we assume the growth rate $V_g = L/t$ (when $t \le 180$ s), which means that wider NRs grow faster than narrower ones. It is also obvious in Fig. 3a that V_g increases with increasing P_{sulfur}, and the overall width distribution shifts to smaller width as P_{sulfur} increases (Fig. 3b), indicating that the smallest width of NR decreases with increasing supersaturation, i.e., shifting from 60–70 nm to 7–10 nm as P_{sulfur} increasing from 7.6×10^{-5} atm to 0.017 atm (see Suppl. Note 1 for more detailed discussion on width distribution).

In crystal growth theory, the growth rate can be described by $V_g = K_g(\Delta\mu/(k_B T))^n$, where K_g is the kinetic factor, $\Delta\mu$ the difference of chemical potentials, k_B the Boltzmann constant, T is the temperature, and n is the order (typically $n = 1$ or 2, corresponding to linear or quadratic growth of nanowires[30]). We consider the following steps for NR growth: i) impingement of S atoms into the liquid Na-Mo-Ni-O droplet from vapor phase due to difference in chemical potentials of S on vapor-liquid boundary, $\Delta\mu_{vl}$, which depends on the droplet diameter, ii) formation of Mo-S motifs and diffusion towards droplet-substrate boundary, and iii) crystallization of the liquid alloy on the substrate under the droplet by precipitation of Mo-S motifs due to chemical potentials difference $\Delta\mu_{ls}$ between the liquid droplet and solid MoS_2 NR, which also depends on droplet diameter. Unlike most

https://doi.org/10.1038/s41467-024-54413-9

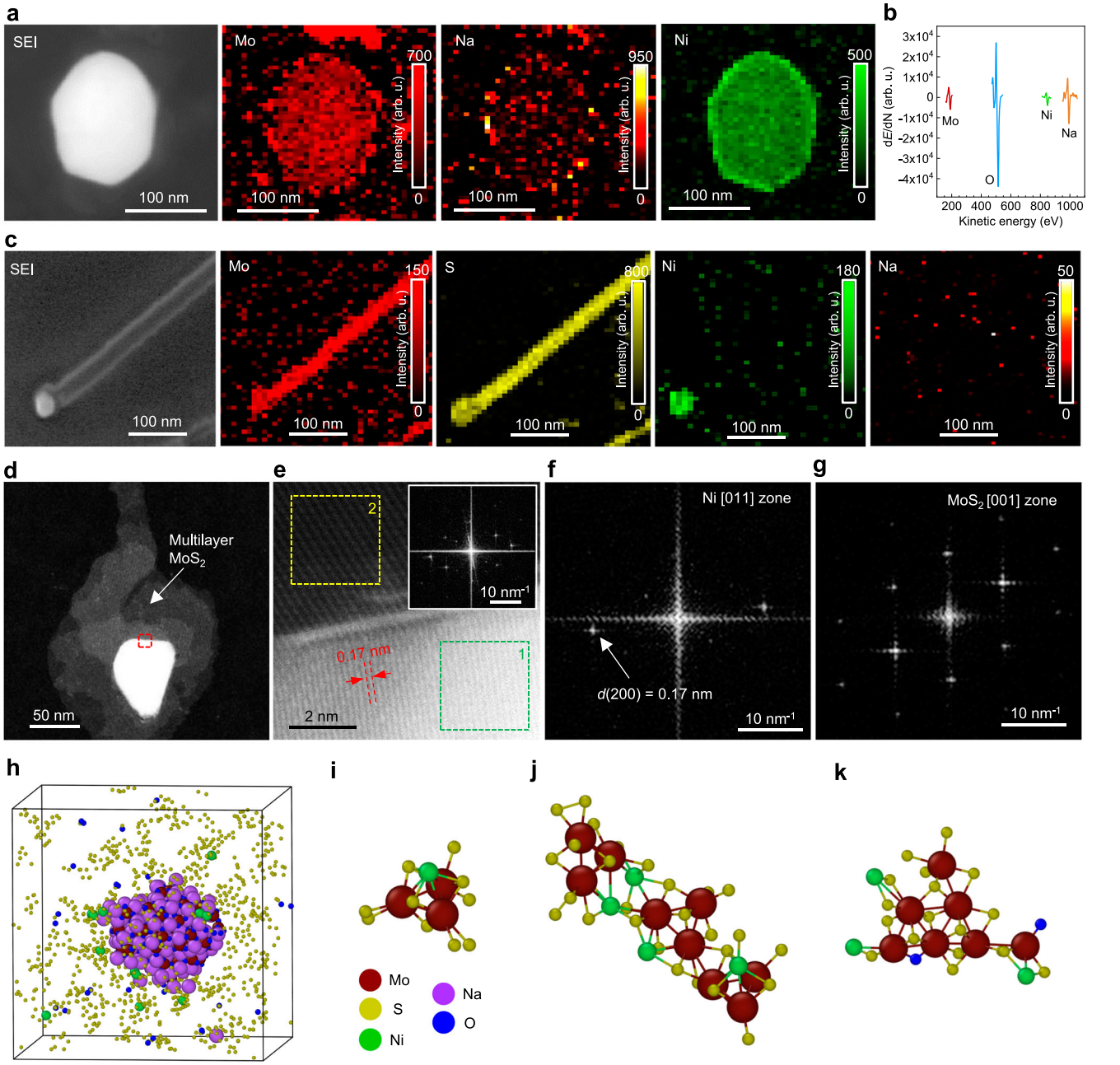

Fig. 2 | Evolution of seed NPs. a AES elemental mapping of Mo, Na, and Ni in a seed NP. SEI stands for secondary electron image. **b** Corresponding AES spectra of Mo (red), Na (orange), Ni (green), and O (blue) in the NP. Note that AES analysis the NPs were deposited on a SiO_2/Si substrate. **c** AES elemental mapping of Mo, S, Ni, and Na of a SL MoS_2 NR including the tip NP, transferred on a SiO_2/Si substrate after growth. The Mo and S signal at the NP tip area come from the multilayers of MoS_2 precipitated from the tip NP during the cooling down (see **d**). The color scales in (**a**) and (**c**) are linear. **d** Low-magnification STEM image of a MoS_2 NR emanating from the NP tip. **e** High resolution HAADF-STEM image of the region indicated by the dashed red box in (**d**), showing the interface between the tip NP and MoS_2. Inset is the FFT pattern of the whole image. **f**, **g** FFT pattern acquired from the dashed green box 1 and dashed yellow box 2 in (**e**), showing Ni [011] zone and MoS_2 [001] zone, respectively. **h** MD simulation of a Na-Mo-Ni-O NP interactions with S atoms, showing separation of Ni atoms from the other nanoparticles atoms after being equilibrated at 650 K for 6 ns. Color code of the atoms: Mo (dark red), S (yellow), Ni (green), Na (purple), O (blue). **i**–**k** Extended simulation of the Na-Mo-Ni-O NP in the S environment for 10 ns at 525 K, showing that Mo atoms in the NP start to form triangular local structural motifs with a Ni atom on the top (**i**), inter-connected triangular Mo local motifs (**j**), and embryo of two-dimensional hexagonal structures (**k**) Source data are provided as a Source Data file.

of the typical nanowire and SL TMD growth, there is no growth through the vapor-solid interface by direct incorporation of S atoms from vapor into the solid MoS_2 NR via terrace/edge impingement since there is no Mo vapor in the surrounding atmosphere. Hence, the only driving force for NR growth is the supersaturation of Mo-S motifs concentration in the droplet relative to solid NR, which elevates due to the impinging of S atoms from vapor phase into droplet. Considering S vapor as an ideal gas, the supersaturation of S atoms in the droplet with diameter (d) according to Gibbs-Thomson effect[30] could be expressed as

$$\Delta\mu_{vl}/(k_B T) = \Delta\mu_{\infty}/(k_B T) - 2\sigma_{vl}\Omega/(d k_B T) \quad (1)$$

https://doi.org/10.1038/s41467-024-54413-9

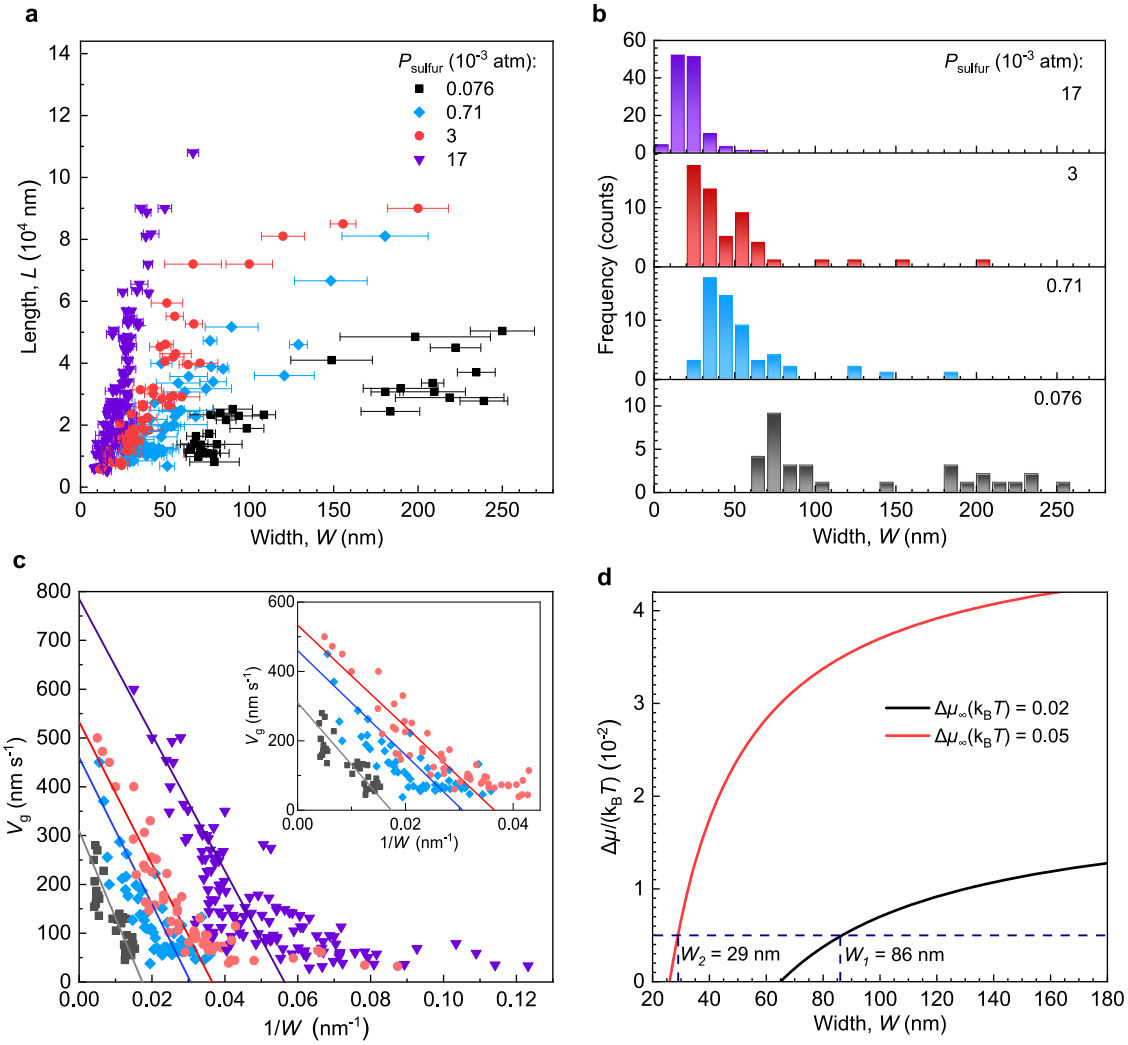

Fig. 3 | Precipitation-driven growth mechanism study. a Statistics of dependence of NR L on W with T_{sulfur} = 130, 170, 200, and 250 °C, corresponding to $P_{sulfur} = 7.6 \times 10^{-5}$ (black symbols), 7.1×10^{-4} (blue symbols), 0.003 (red symbols), and 0.017 atm (purple symbols), respectively. The NRs were grown for 180 s. The L vs W data of the NRs have been collected from three independent growth experiments at a given growth temperature (730 °C) for each P_{sulfur} (T_{sulfur}). The error bars represent the variations of width along the length of each NRs. **b** Histograms of width distribution of MoS_2 NR measured in (**a**), with $P_{sulfur} = 7.6 \times 10^{-5}$ (black), 7.1×10^{-4} (blue), 0.003 (red), and 0.017 atm (purple). **c** Growth rate V_g vs. $1/W$ with different P_{sulfur}. The color code corresponds to (**a**). Solid lines are fitting results using Eq. (2) with $n = 1$. Inset is enlarged view of $P_{sulfur} = 7.6 \times 10^{-5}$, 7.1×10^{-4}, and 0.003 atm. **d** Actual supersaturation $\Delta\mu_{vl}/(k_BT)$ vs. W according to Eq. (1) with $\Delta\mu_\infty/(k_BT) = 0.02$ (black curve) and 0.05 (red curve), corresponding to $P_{sulfur} = 7.6 \times 10^{-5}$ and 0.003 atm. Source data are provided as a Source Data file.

where $\Delta\mu_\infty/(k_BT) = \ln(P_{sulfur}/P_\infty)$ is the supersaturation between vapor and the droplet with infinite interface, P_∞ is the pressure on the infinite boundary of S and droplet, σ_{vl} the surface energy of Ni-Mo alloy (≈1.7 J m^{-2}), Ω is the S atomic volume in the droplet (0.0056 nm^3), $k_B = 1.380649 \times 10^{-23}$ J K^{-1}, and $T = 1003$ K is the synthesis temperature (see Suppl. Note 2 for detailed explanation). Correspondingly, V_g could be expressed as

$$V_g = K_g(\Delta\mu_\infty/(k_BT) - 2\sigma_{vl}\Omega/(dk_BT))^n \quad (2)$$

Furthermore, we found that the width of grown NRs is related to the diameter of the droplets by $d = W/(\sin\alpha) \approx W/0.75$, based on experimental observations of contact angle between NP droplet and the NR (Supplementary Fig. 2b). Hence, we analyzed the plots of V_g vs. $1/W$ for NRs grown under different P_{sulfur} (Fig. 3c). In the lower supersaturation region (i.e., larger W or d), V_g decreases linearly with increasing $1/W$, and each plot could be best fitted using Eq. (2) with $n = 1$, from which nearly constant K_g values for all P_{sulfur} were extracted (Table 1). However, it should be noticed that as supersaturation gets higher, especially for $W < 20$ nm, V_g becomes almost independent of $1/W$. Such a behavior is more dominant as P_{sulfur} gets higher (e.g., $P_{sulfur} = 0.017$ atm), which results in NRs with mostly narrower widths (Fig. 3c). Such a deviation from the Gibbs-Thomson effect could be attributed to the peculiarities of our NR formation. Specifically, in our method the seed droplet is the only source for Mo atoms, whose solubility in the Ni-Mo-O nanoalloy generally depends on the droplet size when $d < 20$ nm, which affects the supersaturation of Mo-S motifs

Table 1 | Kinetic factor (K_g), critical width (W_c) of NRs, and supersaturations at infinite boundary ($\Delta\mu_\infty/(k_BT)$) under different sulfur vapor pressure (P_{sulfur})

P_{sulfur} (atm) / T_{sulfur} (K)	K_g (10^{-5} m s^{-1})	W_c (nm)	$\Delta\mu_\infty/(k_BT)$ ($T = 1003$ K)
6×10^{-5} / 403	1.15	56	0.02
1×10^{-4} / 443	1.09	33	0.04
3×10^{-3} / 473	1.06	26	0.05
1.7×10^{-2} / 523	1.01	17	0.08

in the droplet and thereby on the growth rate. The reduction of the solubility of Mo in the droplet with decrease of droplet size can drive excess precipitation, resulting in increase of the growth rate[40]. Due to the lack of data for this quaternary nanoalloy phase diagram, further study is needed on this scope.

To further validate the growth mechanism of single-crystal SL MoS_2 NRs, as shown in the structural analysis (Fig. 1f, g), we analyzed the growth rate of NRs with different width but grown under the same supersaturation on the vapor-liquid interface. The interceptions of the fitting lines for V_g vs. $1/W$ with the $1/W$-axis in Fig. 3c, where growth rate is zero, provide critical widths $W_c = 2\sigma_{vl}\Omega/\Delta\mu_\infty$ under different P_{sulfur} according to Gibbs-Thomson model. For given values of W_c, we obtained the corresponding values of supersaturation $\Delta\mu_\infty/(k_BT)$ for different P_{sulfur} from Eq. (2) (Table 1). Using Eq. (1), the width dependence of actual supersaturation $\Delta\mu_{vl}/(k_BT)$ for $\Delta\mu_\infty/(k_BT) = 0.02$ and 0.05 were plotted (Fig. 3d), from which we found two width values $W = 86$ and 27 nm, with a same actual supersaturation, i.e., $\Delta\mu_{vl}/(k_BT) = 0.005$. They correspond to growth rate $V_g = 80$ and 25 nm s^{-1}, respectively, according to V_g vs. $1/W$ experimental graph in Fig. 3c. The results indicate that even though the interface area under the droplet of the wider NR (≈7400 nm^2) is about 10 times larger than that of the narrower one (≈730 nm^2), the V_g is only ≈ 3 times higher, which excludes the monocentric nucleation-mediated growth that could result in observed single crystal NRs. As shown above the growth rate, $V_g = K_g(\Delta\mu/(k_BT))$, depends linearly on $\Delta\mu$ with nearly constant kinetic factor K_g for all P_{sulfur} (Fig. 3c and Table 1), i.e. within the experimental range of applied supersaturations ($\Delta\mu < 0.25k_BT$) K_g can be considered independent of $\Delta\mu$. The linear dependence of V_g on $\Delta\mu$, as an experimental criterion, suggests that the formation of single crystal NR is the result of a continuous growth[41] through the attachment of atoms from the supersaturated droplet alloy to the NR edges with atomic steps/kinks as growth sites of the SL MoS_2 nucleus that grows axially under the droplet.

Growth of other TMD NRs

Beyond MoS_2, we used the two-step method above to grow other SL TMD NRs including $MoSe_2$, WS_2, and WSe_2 on F-mica substrates. $MoSe_2$ NRs were also precipitated from pre-deposited Na-Mo-Ni-O seed NPs, driven by selenium vapor (Supplementary Fig. 13). However, W-based TMD NRs are grown from pre-deposited seed NPs composed of Na-W-Mg-O, in which Mg plays a similar role as Ni (Supplementary Figs. 14–16), which points out the importance of nanoalloy composition.

Width-dependent optical properties of NRs

Next, we attempted to reveal whether the width as an additional degree of freedom enabled by NR geometry could endow tunable intrinsic properties of NRs. We found that the optical properties of NRs are influenced by their width. Specifically, at room temperature, the SL MoS_2 NRs show width-dependent photoluminescence (PL) from the A-exciton (Fig. 4a), which is further corroborated on the nanoscale with nano-PL characterization of individual NRs using tip-enhanced PL (TEPL) measurement. (Supplementary Fig. 17). The PL of the A-exciton blueshifts as the width of the NR decreases, similar to the trend observed in ref. 25. The microscopic origins of such width-dependent PL of the NRs could arise to an interplay between interior states and edge states. The energy blueshift is most pronounced in the range of 50–20 nm, where a linear dependence on $1/W^2$ is shown (inset of Supplementary Fig. 17c), indicating that the energy shift is due to the weak confinement on exciton center-of-mass in an infinite potential well[42–44]; while for NRs with width >50 nm, the energy shift could be dominant by the edge states, where strain relaxation, chemical termination, and or interaction with the substrate result in localized states as previously reported in nearfield studies of 2D crystallites[45,46]. Preliminary measurements show that such edge states may also exists in the MoS_2 NRs (Supplementary Fig. 18), and future measurements will focus on unraveling how these states contribute to the width-dependent effects observed here.

Quantum emission from strain-engineered TMD NRs

Further, strain engineering has been widely used for tailoring excitonic light-matter interactions and deterministically creating localized electronic states in 2D semiconductors[47–51] for potential applications. For our SL NR systems, analysis of atomic resolution HAADF-STEM imaging (Supplementary Fig. 19) reveals that they can accommodate from -14% (compressive) to +14% (tensile) strains. Optically, the SL TMD NRs preserve the strain-tunable intense excitonic light-matter interactions that are expected from SL 2D semiconductors[52]. Exploiting the observed mechanical robustness, we transferred as grown SL MoS_2 and WSe_2 NRs onto arrays of gold nanocones (inset of Fig. 4b)[49,50] to realize strain-induced localized states. The gold nanocones have an average height and base diameter of ≈ 100 nm, and a radius of curvature at the apex of ≈ 5 nm (Supplementary Fig. 20). For a SL MoS_2 NR with a width of 100 nm, the strain induced by being draped over the gold nanocone (Fig. 4b, red curve) generates a pronounced localized exciton state at 1.77 eV that is ≈ 2 × brighter with a narrower linewidth (≈25 meV) than the PL of the free A exciton at 1.97 eV. In contrast, such a strong feature is absent in the PL spectrum acquired from the unstrained NR (Fig. 4b, blue curve). Similar strain-localization of excitons at the same energy (1.77 eV) in SL MoS_2 NRs are observed at room temperature in nanoscale regions directly surrounding a NR draped over a nanocone by nano-PL imaging (Supplementary Fig. 21). In the time evolution of the PL spectra from the strained region (inset of Fig. 4b), the PL intensity and energy of the A exciton 1.97 eV does not show any temporal variation, which is expected for a state that is not localized; in contrast, emission from the strained region exhibits spectral wandering (i.e., random jumps to different energies) and intensity fluctuations on the timescale of seconds, which are both signatures of highly localized quantum dot-like states that can generate single photons[48]. This report introduces purely strain-induced quantum dot-like states in single-layer MoS_2 without the use of ion irradiation[53] (see Suppl. Note 3 for more detailed discussion).

Finally, using the same strain-engineering method on SL WSe_2 NRs, we confirm the ability to fabricate single photon emitters (SPEs) in the more confined geometry of the NRs. Figure 4c shows that bright, narrowband emitters emerge from localized strained regions of a ≈ 100 nm-wide SL WSe_2 NR that is draped over a similar array of gold nanocones (Supplementary Fig. 22a). Nano-PL imaging (inset of Fig. 4c, Supplementary Fig. 22b) reveals a series of bright emissive spots that each correspond to a region where the SL WSe_2 NR is draped over an individual cone. The selected spectrum in Fig. 4c is from the cone site that is marked in the inset. Similar spectra are observed from the other cone-induced strained sites, with emitter energies ranging from 1.6–1.7 eV (Supplementary Fig. 22b, c; 40–50 meV lower than the free exciton in unstrained WSe_2 at 4 K). The linewidths of the strain-induced emitters are >10 × narrower, and their intensities are 100–1000 × brighter than the localized state in the SL MoS_2 NR (Fig. 4b). The much larger intensity of these emitters permits measurement of the second-order autocorrelation function $g^{(2)}(\tau)$ using a Hanbury-Brown-Twiss interferometer (see Methods), which reveals clear photon antibunching with a purity of 80%–90% (Fig. 4d, Supplementary Fig. 23). The demonstration of antibunching in a TMD NR system sets the stage for further research into the width-dependent optical properties of the NRs (i.e., Fig. 4a) and the use of local strain engineering, specific to the NR geometry, to potentially create more homogenous populations of 2D semiconductor-based SPEs for broadscale quantum photonic applications.

In conclusion, we developed a facile method for direct growth of single-crystal SL TMD NRs, which allows controllable downscaling NRs widths down to 7 nm. Deconvolution of seed NP formation and NR

https://doi.org/10.1038/s41467-024-54413-9

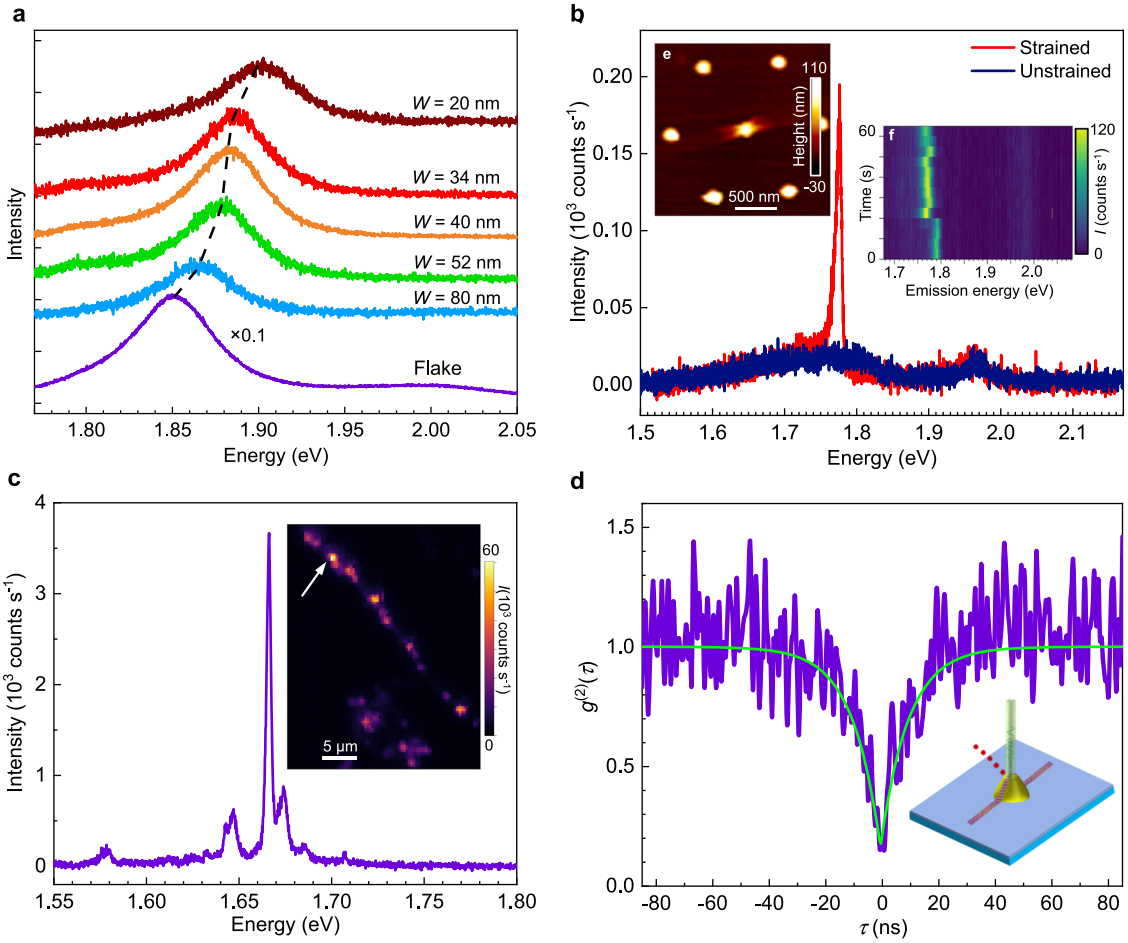

Fig. 4 | Width-dependent PL and quantum light emission from strained SL MoS_2 and WSe_2 NRs. a PL spectra of SL MoS_2 flake (purple curve) and NRs with width of 80 (blue curve), 52 (green curve), 40 (orange curve), 34 (red curve), and 20 nm (dark red curve) at room temperature. (**b**) PL spectra of a MoS_2 NR draped over an Au nanocone, from the region over the cone (strained, red curve) and unstrained region (dark blue curve) at $T = 4$ K. Inset (**e**): AFM topography of the SL MoS_2 NR draped over a cone. Inset (**f**): time-series of the PL spectra from strained region. **c** PL spectrum of one of the strained regions (indicated by the white arrow in the inset) of a SL WSe_2 NR on Au nanocones (see Supplementary Fig. 20) at $T = 4$ K. Inset: Mapping of integrated PL intensity from the WSe_2 NR. The color scales in (**b**) and (**c**) are linear. **d** $g^{(2)}(\tau)$ measurement of the emitter in (**c**) at 1.67 eV. The fitting of the $g^{(2)}(\tau)$ curve (green curve)[60] gives a single photon purity of 81%. Inset is the illustration of quantum light emission generated from strain-engineering NRs by nanocones. Source data are provided as a Source Data file.

growth process allows independent control over the width of the NRs via diameter of seed NPs. Unlike other 1D nanostructures such as whiskers and nanowires, we reveal a continuous growth mechanism for NRs with the growth rate that depends linearly on the reciprocal width of NRs due to the Gibbs-Thomson effect. The NRs show significant mechanical robustness that can accommodate up to ≈ 14% compression and tensile strain. The strain-induced localized quantum dot like states emit single photons in TMD NRs. The initial results on the SL WSe_2 nanoribbons demonstrate the great potential to realize precisely localized quantum light sources in NRs of TMDs for quantum optoelectronic applications.

Methods

Material synthesis

SL MoS_2 NRs were synthesized in a tube furnace system similar to ref. 18. Specifically, two separate argon gas lines are connected to the tube furnace, in which one directly goes to the reaction chamber (called F_{Ar}) while the other goes through a small bubbler, containing 2 mL of DI water to produce moisturized Ar (called $F_{Ar/H2O}$) before reaching the reaction tube, resulting in a moisturized Ar flow with ≈ 3000 ppm H_2O. In the first step, a mixture of MoO_2, NaBr, and Ni powder at a certain weight ratio was placed in an alumina boat, and a piece of freshly cleaved F-mica was placed ≈ 3 mm above the precursor. The precursor was heated to 730 °C under a gas flow of 40 cm^3 STP min^{-1} of F_{Ar} combined with 40 cm^3 STP min^{-1} of $F_{Ar/H2O}$ to allow seed NPs deposited on the F-mica. In the second step, the F-mica with deposited seed NPs was placed in another clean alumina boat and heated to 730–770 °C at the center of the tube furnace, and meanwhile, sulfur powder, placed at the upper stream, was heated separately by a heating belt to 130–270 °C to provide sulfur vapor, carried by a dry Ar flow of 80 cm^3 STP min^{-1} to sulfurize seed NPs. For the growth of $MoSe_2$ NRs, the same seed NPs were used, while selenium powders were heated to 350–420 °C to provide selenium vapor carried by a combination of 80 cm^3 STP min^{-1} Ar and 6 cm^3 STP min^{-1} H_2. For the growth of WS_2 and WSe_2 NRs, seed NPs were deposited from a mixture of WO_2, NaBr, and Mg precursor.

Characterization

The as-synthesized MoS_2 NRs were characterized using scanning electron microscopy (SEM, FEI QUANTA FEG 650, operating at 5 kV), atomic force microscopy (AFM, Bruker Dimension Icon), Raman spectroscopy (Renishaw inVia Raman microscope, with 1800 grooves mm^{-1} grating and a 532 nm laser, 1 mW laser power, as excitation source). AES was conducted in a PHI 700 scanning Auger nanoprobe

(Physical Electronics) at a working voltage and current of 10 kV and 10 nA. The samples for TEM and STEM characterization were prepared using a wet transfer process. Poly(methyl methacrylate) (PMMA) 495A4 (MicroChem) is first spun onto the F-mica substrate with monolayer crystals at 3500 rounds min^{-1} for 60 s. The PMMA-coated substrate was then floated on deionized (DI) water to detach the PMMA film with the ribbons from the substrate. The floating PMMA film was scooped onto a 3 nm-thick amorphous carbon film supported by a Au TEM grid, which was subsequently soaked in acetone for 12 h to remove PMMA and get a clean sample surface. The transferred samples were finally annealed at 200 °C in vacuum to get rid of the solvent. STEM images were acquired at 60 kV using a Nion UltraSTEM equipped with a probe aberration corrector (the convergence angle was 31 mrad). The inner and outer collection angle of the HAADF detector were 86 and 200 mrad, respectively. To enhance the signal-to-noise ratio, atomic-resolution STEM images were blurred using a 2D Gaussian distribution.

Device fabrication

The FET devices were fabricated using electron-beam (e-beam) lithography patterning, performed by Nanobeam n64 Electron Beam Writer system. The electron beam was operated at an accerlating voltage of 80 kV. Metal electrodes of Bi/Au (20 nm/40 nm) were deposited on top of MoS_2 NRs in Angstrom EvoVac Deposition system, the deposition vacuum level is $<5 \times 10^{-7}$ Torr. Transport measurements were performed in a CTI-Cryogenics Model 22 Refrigerator using a Keysight B1500A Semiconductor Device Parameter Analyzer.

MD simulations

MD simulations were carried out using LAMMPS[54], with a recent universal neural network interatomic potential called PFP as implemented on the Matlantis™ platform[55]. PFP has been demonstrated with DFT-level accuracy and has been successfully applied in modeling a wide range of materials. Our MD simulations employed the v4.0.0 version of PFP with the "CRYSTAL_U0" mode. The initial structures of nanoparticles were prepared using the packmol softwar[56]. Nanoparticle with oxygen contains 500 atoms, with 143 Na atoms, 57 Mo atoms, 14 Ni atoms and 286 Oxygen atoms. Nanoparticle without oxygen contains 133 Na atoms, 33 Mo atoms, and 13 Ni atoms. The initial configuration was equilibrated at 300 K for 1 ns, using constant temperature, constant volume MD simulations (NVT), with sufficient vacuum regions (at least >24 Å, the effective interaction range from the graph convolution operations) to avoid image interactions. S atoms were randomly inserted into the simulation box to observe their interactions with nanoparticles. All subsequent simulations at different temperatures were carried out under NVT conditions. Structures were visualized using the Ovito software[57].

Strain analysis

First, we performed filtering to improve the signal-to-noise ratio in the atomic resolution STEM images. Fast Fourier transformation (FFT) has been performed on the red boxes in Supplementary Fig. 19c, d. Reciprocal space around the first-order Bragg peaks is chosen to conduct the inverse FFT, which effectively enhances the contrast of atomic columns and facilitates further detection. The second step is to locate the positions of all the atomic columns that are of interest in the filtered HAADF-STEM images, as shown in Supplementary Fig. 19e, f. The peak finding algorithm offered by the ATOMAP Python library[58] is leveraged to identify initial atomic positions, with the relative intensity threshold and minimum peak separation serving as inputs. The initial positions are further refined, first by determining the center-of-mass and then by two-dimensional (2D) Gaussian peak fitting. This allows for a precise determination of the 2D atomic column positions. Third, two sets of non-parallel planes are selected to measure the relative variations in plane distance compared to the reference value obtained away from the MoS_2 kinks at the middle section in Supplementary Fig. 19b. Previously, the TopoTEM Python library[59] has been employed for strain calculation via interplanar distance variation with the reference value in HAADF-STEM images for crystal with orthogonal axes. Building upon this, we perform a detailed basis vector transformation from inter-planar direction to orthogonal basis in MoS_2 strain study. This enables the computation of MoS_2 displacement field on an orthogonal basis, which subsequently leads to the calculation of in-plane hydrostatic strain mapping results, as shown in Supplementary Fig. 19g, h. The in-plane hydrostatic strain variation along the lines depicted in Supplementary Fig. 19e, f has been calculated. The average value is plotted along the diagonal direction, which reveals a higher magnitude of hydrostatic strain closer to the MoS_2 kinks, as shown in Supplementary Fig. 19i.

Nanocone fabrication

Substrates with nanocone stressor arrays were fabricated according to the process outlined by Yanev et al.[50]. A base layer of gold was evaporated onto a silicon wafer, followed by electron-beam lithography and Al_2O_3 deposition. After lift-off, disks of alumina were left behind, which served as a hard mask during the final argon ion milling step. See ref. 44 for more details and discussion of the fabrication process.

NR transfer on nanocones

A piece of polydimethylsiloxane (PDMS) film ($1 \times 1\ cm^2$, Gel-Pek) is first stamped onto the as-grown NRs on F-mica substrate. The NRs are detached from the substrate and picked up by PDMS film assisted by DI water. The PDMS film with NRs is then stamped on a glass slide, which is subsequently mounted on a 2D materials transfer stage (HQ Graphene) with targeting substrate with fabricated Au nanocones. Specific NR is aligned on Au cone arrays through an optical microscope and placed on top of them. Finally, the stage is heated to 65 °C to lift off the PDMS film, leaving the NR on Au nanocones.

TEPL measurement

Near-field optical measurements were carried out using a commercially available AFM system (OmegaScope; Horiba Scientific) coupled to a Raman spectrometer (LabRAM HR Evolution; Horiba Scientific). In this setup, a 594 nm laser was focused onto the tip of a gold coated AFM probe (AppNano Omni™ TERS-NC-Au) after passing through a long working distance microscope objective (100×, 0.7 NA) mounted at an angle (25° from horizontal). Enhanced PL from the sample was collected through the same objective. Spectra were taken with the tip in contact and also slightly retracted from the surface at each location. This allows for a pixel-wise subtraction of the far-field background, which was used to produce the TEPL maps shown in this work.

Low-temperature PL measurement

Low-temperature spectroscopy was conducted using a homebuilt confocal microscope. Light is focused on samples mounted in a Montana Instruments S50 cryostat using a Nikon Plan Fluor 40× long working distance objective. Excitation for MoS_2 was done with a 532 nm (Cobalt Samba™ 100) diode laser. Laser power on the sample was measured at 20 μW. The excitation source used for the WSe_2 spectra and $g^{(2)}(\tau)$ measurement was a 78 MHz pulsed supercontinuum laser (NKT Photonics SuperK EXTREME). An excitation wavelength of 532 nm was selected using an acoustic optical modulator and a tunable short-pass filter. The laser power on the sample was 60 nW. Integrated PL intensity was collected with a Micro Photon Devices (MPD) APD, and spectra were collected with a Horiba iHR320 spectrometer and a cooled Andor iDus CCD camera.

Data availability

The data that support the findings of this study are available from the corresponding authors upon request. Source data are provided with this paper.

References

1. Giamarchi, T. *Quantum Physics in One Dimension* 1st edn, Vol. 442 (Oxford University Press, 2003).
2. Huang, S. et al. Classical Coulomb blockade of a silicon nanowire dot. *Appl. Phys. Lett.* **92**, 213110 (2008).
3. Niu, S. et al. Giant optical anisotropy in a quasi-one-dimensional crystal. *Nat. Photonics* **12**, 392–396 (2018).
4. Noguchi, R. et al. A weak topological insulator state in quasi-one-dimensional bismuth iodide. *Nature* **566**, 518–522 (2019).
5. Harutyunyan, A. R. Carbon nanotubes: helicity origin and envisioned applications. *Nano Today* **56**, 102248 (2024).
6. Rizzo, D. J. et al. Topological band engineering of graphene nanoribbons. *Nature* **560**, 204–208 (2018).
7. Kolmer, M. et al. Rational synthesis of atomically precise graphene nanoribbons directly on metal oxide surfaces. *Science* **369**, 571–575 (2020).
8. Wang, H. S. et al. Towards chirality control of graphene nanoribbons embedded in hexagonal boron nitride. *Nat. Mater.* **20**, 202–207 (2021).
9. Lyu, B. et al. Catalytic growth of ultralong graphene nanoribbons on insulating substrates. *Adv. Mater.* **34**, 2200956 (2022).
10. Lyu, B. et al. Graphene nanoribbons grown in hBN stacks for high-performance electronics. *Nature* **628**, 758–764 (2024).
11. Li, Y., Zhou, Z., Zhang, S. & Chen, Z. MoS_2 nanoribbons: high stability and unusual electronic and magnetic properties. *J. Am. Chem. Soc.* **130**, 16739–16744 (2008).
12. Yue, Q. et al. Bandgap tuning in armchair MoS_2 nanoribbon. *J. Phys. Condens. Matter* **24**, 335501 (2012).
13. Cai, Y., Zhang, G. & Zhang, Y.-W. Polarity-reversed robust carrier mobility in monolayer MoS_2 nanoribbons. *J. Am. Chem. Soc.* **136**, 6269–6275 (2014).
14. Hu, T., Zhou, J., Dong, J. & Kawazoe, Y. Electronic and magnetic properties of armchair MoS_2 nanoribbons under both external strain and electric field, studied by first principles calculations. *J. Appl. Phys.* **116**, 064301 (2014).
15. Ouyang, F. et al. Hydrogenation-induced edge magnetization in armchair MoS2 nanoribbon and electric field effects. *Appl. Phys. Lett.* **104**, 071901 (2014).
16. Balandin, A. A., Kargar, F., Salguero, T. T. & Lake, R. K. One-dimensional van der Waals quantum materials. *Mater. Today* **55**, 74–91 (2022).
17. Chen, S. et al. Monolayer MoS_2 nanoribbon transistors fabricated by scanning probe lithography. *Nano Lett.* **19**, 2092–2098 (2019).
18. Li, X. et al. Nickel particle-enabled width-controlled growth of bilayer molybdenum disulfide nanoribbons. *Sci. Adv.* **7**, abk1892 (2021).
19. Deng, Y. et al. Lithography-free, high-density $MoTe_2$ nanoribbon arrays. *Mater. Today* **58**, 8–17 (2022).
20. Li, S. et al. Vapour–liquid–solid growth of monolayer MoS_2 nanoribbons. *Nat. Mater.* **17**, 535–542 (2018).
21. Chen, T. et al. Controlled growth of atomically thin $MoSe_2$ films and nanoribbons by chemical vapor deposition. *2D Mater.* **6**, 025002 (2019).
22. Aljarb, A. et al. Ledge-directed epitaxy of continuously self-aligned single-crystalline nanoribbons of transition metal dichalcogenides. *Nat. Mater.* **19**, 1300–1306 (2020).
23. Yang, P. et al. Epitaxial growth of inch-scale single-crystal transition metal dichalcogenides through the patching of unidirectionally orientated ribbons. *Nat. Commun.* **13**, 3238 (2022).
24. Xue, G. et al. WS_2 ribbon arrays with defined chirality and coherent polarity. *Science* **384**, 1100–1104 (2024).
25. Chowdhury, T. et al. Substrate-directed synthesis of MoS_2 nanocrystals with tunable dimensionality and optical properties. *Nat. Nanotechnol.* **15**, 29–34 (2020).
26. Baker, R. T. K., Barber, M. A., Harris, P. S., Feates, F. S. & Waite, R. J. Nucleation and growth of carbon deposits from the nickel catalyzed decomposition of acetylene. *J. Catal.* **26**, 51–62 (1972).
27. Dresselhaus, M. S., Dresselhaus, G., Sugihara, K., Spain, I. L. & Goldberg, H. A. In, *Graphite Fibers and Filaments*. 12–34 (Springer Berlin Heidelberg, Berlin, Heidelberg, 1988).
28. Harutyunyan, A. R. et al. Preferential growth of single-walled carbon nanotubes with metallic conductivity. *Science* **326**, 116–120 (2009).
29. Givargizov, E. I. & Sheftal, N. N. Morphology of silicon whiskers grown by the VLS-technique. *J. Cryst. Growth* **9**, 326–329 (1971).
30. Givargizov, E. I. Fundamental aspects of VLS growth. *J. Cryst. Growth* **31**, 20–30 (1975).
31. Schubert, L. et al. Silicon nanowhiskers grown on ⟨111⟩ Si substrates by molecular-beam epitaxy. *Appl. Phys. Lett.* **84**, 4968–4970 (2004).
32. Dubrovskii, V. G. et al. Diffusion-induced growth of GaAs nanowhiskers during molecular beam epitaxy: theory and experiment. *Phys. Rev. B* **71**, 205325 (2005).
33. Kikkawa, J., Ohno, Y. & Takeda, S. Growth rate of silicon nanowires. *Appl. Phys. Lett.* **86**, 123109 (2005).
34. Kodambaka, S., Tersoff, J., Reuter, M. C. & Ross, F. M. Diameter-independent kinetics in the vapor-liquid-solid growth of Si nanowires. *Phys. Rev. Lett.* **96**, 096105 (2006).
35. Wu, Y. et al. Controlled growth and structures of molecular-scale silicon nanowires. *Nano Lett.* **4**, 433–436 (2004).
36. Ji, Q. et al. Epitaxial monolayer MoS_2 on mica with novel photoluminescence. *Nano Lett.* **13**, 3870–3877 (2013).
37. Li, X. et al. Surfactant-mediated growth and patterning of atomically thin transition metal dichalcogenides. *ACS Nano* **14**, 6570–6581 (2020).
38. Shen, P.-C. et al. Ultralow contact resistance between semimetal and monolayer semiconductors. *Nature* **593**, 211–217 (2021).
39. Liu, X. et al. The critical role of electolyte gating on the hydrogen evolution performance of monolayer MoS_2. *Nano Lett.* **19**, 8118–8124 (2019).
40. Harutyunyan, A. R. et al. Reduced carbon solubility in Fe nanoclusters and implications for the growth of single-walled carbon nanotubes. *Phys. Rev. Lett.* **100**, 195502 (2008).
41. Kashchiev, D. In, *Nucleation* 391–409 (Butterworth-Heinemann, Oxford, 2000).
42. Jia, G. Y. et al. Excitonic quantum confinement modified optical conductivity of monolayer and few-layered MoS_2. *J. Mater. Chem. C.* **4**, 8822–8828 (2016).
43. Woggon, U. In, *Optical Properties of Semiconductor Quantum Dots*. 43–101 (Springer Berlin Heidelberg, Berlin, Heidelberg, 1997).
44. Wei, G. et al. Size-tunable lateral confinement in monolayer semiconductors. *Sci. Rep.* **7**, 3324 (2017).
45. Bao, W. et al. Visualizing nanoscale excitonic relaxation properties of disordered edges and grain boundaries in monolayer molybdenum disulfide. *Nat. Commun.* **6**, 7993 (2015).
46. Kastl, C. et al. The important role of water in growth of monolayer transition metal dichalcogenides. *2D Mater.* **4**, 021024 (2017).
47. Branny, A., Kumar, S., Proux, R. & Gerardot, B. D. Deterministic strain-induced arrays of quantum emitters in a two-dimensional semiconductor. *Nat. Commun.* **8**, 15053 (2017).
48. Azzam, S. I., Parto, K. & Moody, G. Prospects and challenges of quantum emitters in 2D materials. *Appl. Phys. Lett.* **118**, 240502 (2021).
49. Darlington, T. P. et al. Imaging strain-localized excitons in nanoscale bubbles of monolayer WSe_2 at room temperature. *Nat. Nanotechnol.* **15**, 854–860 (2020).
50. Yanev, E. S. et al. Programmable nanowrinkle-induced room-temperature exciton localization in monolayer WSe_2. *Nat. Commun.* **15**, 1543 (2024).

51. Chowdhury, T. et al. Anomalous room-temperature photoluminescence from nanostrained $MoSe_2$ monolayers. *ACS Photonics* **8**, 2220–2226 (2021).
52. Peng, Z., Chen, X., Fan, Y., Srolovitz, D. J. & Lei, D. Strain engineering of 2D semiconductors and graphene: from strain fields to band-structure tuning and photonic applications. *Light Sci. Appl.* **9**, 190 (2020).
53. Klein, J. et al. Engineering the luminescence and generation of indivitual defect emitters in atomically thin MoS_2. *ACS Photonics* **8**, 669–677 (2021).
54. Thompson, A. P. et al. LAMMPS - a flexible simulation tool for particle-based materials modeling at the atomic, meso, and continuum scales. *Comput. Phys. Commun.* **271**, 108171 (2022).
55. Takamoto, S. et al. Towards universal neural network potential for material discovery applicable to arbitrary combination of 45 elements. *Nat. Commun.* **13**, 2991 (2022).
56. Martínez, L., Andrade, R., Birgin, E. G. & Martínez, J. M. PACKMOL: A package for building initial configurations for molecular dynamics simulations. *J. Comput. Chem.* **30**, 2157–2164 (2009).
57. Stukowski, A. Visualization and analysis of atomistic simulation data with OVITO–the open visualization tool. *Model. Simul. Mater. Sci. Eng.* **18**, 015012 (2010).
58. Nord, M., Vullum, P. E., MacLaren, I., Tybell, T. & Holmestad, R. Atomap: a new software tool for the automated analysis of atomic resolution images using two-dimensional Gaussian fitting. *Adv. Struct. Chem. Imaging* **3**, 9 (2017).
59. O'Connell, E. N. et al. TopoTEM: A python package for quantifying and visualizing scanning transmission electron microscopy data of polar topologies. *Microsc. Microanal.* **28**, 1444–1452 (2022).
60. Exarhos, A. L., Hopper, D. A., Grote, R. R., Alkauskas, A. & Bassett, L. C. Optical signatures of quantum emitters in suspended hexagonal boron nitride". *ACS Nano* **11**, 3328–3336 (2017).

Acknowledgements

A.R.H. and X.L. thank Masahiko Izumi for supporting the research. A.R.H. thanks Ksenia V. Bets for illustration of growth. X.L. thanks Xinting Shuai for partially helping synthesis. The authors thank Dr. Baichang Li for electrical measurements. STEM characterization was conducted as part of a user project at the Center for Nanophase Materials Sciences, which is a US Department of Energy, Office of Science User Facility at Oak Ridge National Laboratory. AFM and AES measurements were performed at the Stanford Nano Shared Facilities (SNSF) RRID:SCR_023230, supported by the National Science Foundation under award ECCS-2026822.

Author contributions

A.R.H. conceptualized and designed research and suggested growth mechanism. A.R.H. and X.L. planned the experiments and studied the growth mechanism. X.L. developed the synthesis method. Sh.W. and L.M.S. contributed to the NR synthesis. X.L. and Sh.W. developed NR transferring method. P.J.S., J.H., and A.R.H. initiated QE research. P.J.S. and N.B. planned the QE research. E.Y. and P.J.S. fabricated the nanocones and performed near-field measurements. S.W., J.S., M.S., and N.B. performed low-temperature QE property study. Q.-J.L. and J.L. performed the MD simulation. R.R.U. performed STEM imaging. Sh.W. performed AFM measurement. Y.S., Y.Z., and Y.Y. performed strain analysis. A.R.H. and X.L. drafted the manuscript. All the authors contributed to the analysis of data and writing the manuscript.

Competing interests

The authors declare no competing interests.

Additional information

Supplementary information The online version contains supplementary material available at https://doi.org/10.1038/s41467-024-54413-9.

Correspondence and requests for materials should be addressed to Avetik R. Harutyunyan.

Peer review information *Nature Communications* thanks Zhiwen Shi and the other, anonymous, reviewers for their contribution to the peer review of this work. A peer review file is available.

Supplementary Information

Width-dependent continuous growth of atomically thin quantum nanoribbons from nanoalloy seeds in chalcogen vapor

*Xufan Li[1†], Samuel Wyss[2†], Emanuil Yanev[3†], Qing-Jie Li[4,5], Shuang Wu[1], Yongwen Sun[6,7], Raymond R. Unocic[8‖], Joseph Stage[2], Matthew Strasbourg[2], Lucas M. Sassi[1‡], Yingxin Zhu[6,7], Ju Li[4,5], Yang Yang[6,7], James Hone[3], Nicholas Borys[2], P. James Schuck[3], Avetik R. Harutyunyan[1]**

[1]Honda Research Institute USA, Inc., San Jose, CA, 95134, USA.

[2]Department of Physics, Montana State University, Bozeman, MT, 59717, USA.

[3]Mechanical Engineering Department, Columbia University, New York, NY, 10025, USA.

[4]Department of Nuclear Science and Engineering, Massachusetts Institute of Technology, Cambridge, MA, 02139, USA.

[5]Department of Materials Science and Engineering, Massachusetts Institute of Technology, Cambridge, MA, 02139, USA.

[6]Department of Engineering Science and Mechanics, The Pennsylvania State University, University Park, PA, 16802, USA.

[7]Materials Research Institute, The Pennsylvania State University, University Park, PA, 16802, USA.

[8]Center for Nanophase Materials Sciences, Oak Ridge National Laboratory, Oak Ridge, TN, 37831, USA.

[‖]Present address: Department of Materials Science and Engineering, North Carolina State University, Raleigh, NC, 27695, USA.

[‡]Present address: Department of Physics, National University of Singapore, Singapore, 117551, Singapore.

*Corresponding author: aharutyunyan@honda-ri.com

[†]These authors contributed equally.

Supplementary Figures

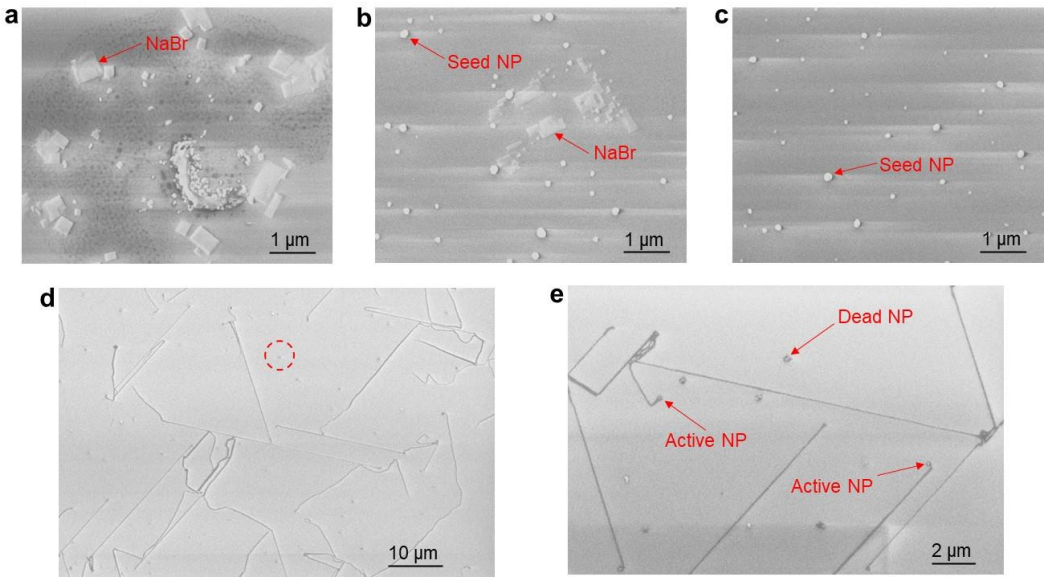

Supplementary Fig. 1. SEM images of seed NPs and MoS_2 NRs grown on F-mica. (**a**–**c**) SEM image showing deposition results from step 1 under (a) dry Ar flow and moisturized Ar flow with moisture content of (b) 1000 ppm and (c) 3000 ppm. Without moisture, no Na-Mo-Ni-O seed NPs but only NaBr was deposited on the F-mica substrate; a lower moisture content resulted in the deposition of both NaBr crystals and seed NPs, while a higher moisture content results in only seed NPs. (**d**) Low magnification SEM image showing as-grown NRs and seed NPs that did not grow into NRs. (**e**) Enlarged view SEM image, highlighting as-grown NRs with NPs remaining on the tip after growth (active NP), and NPs that did not grow into NRs (dead NP).

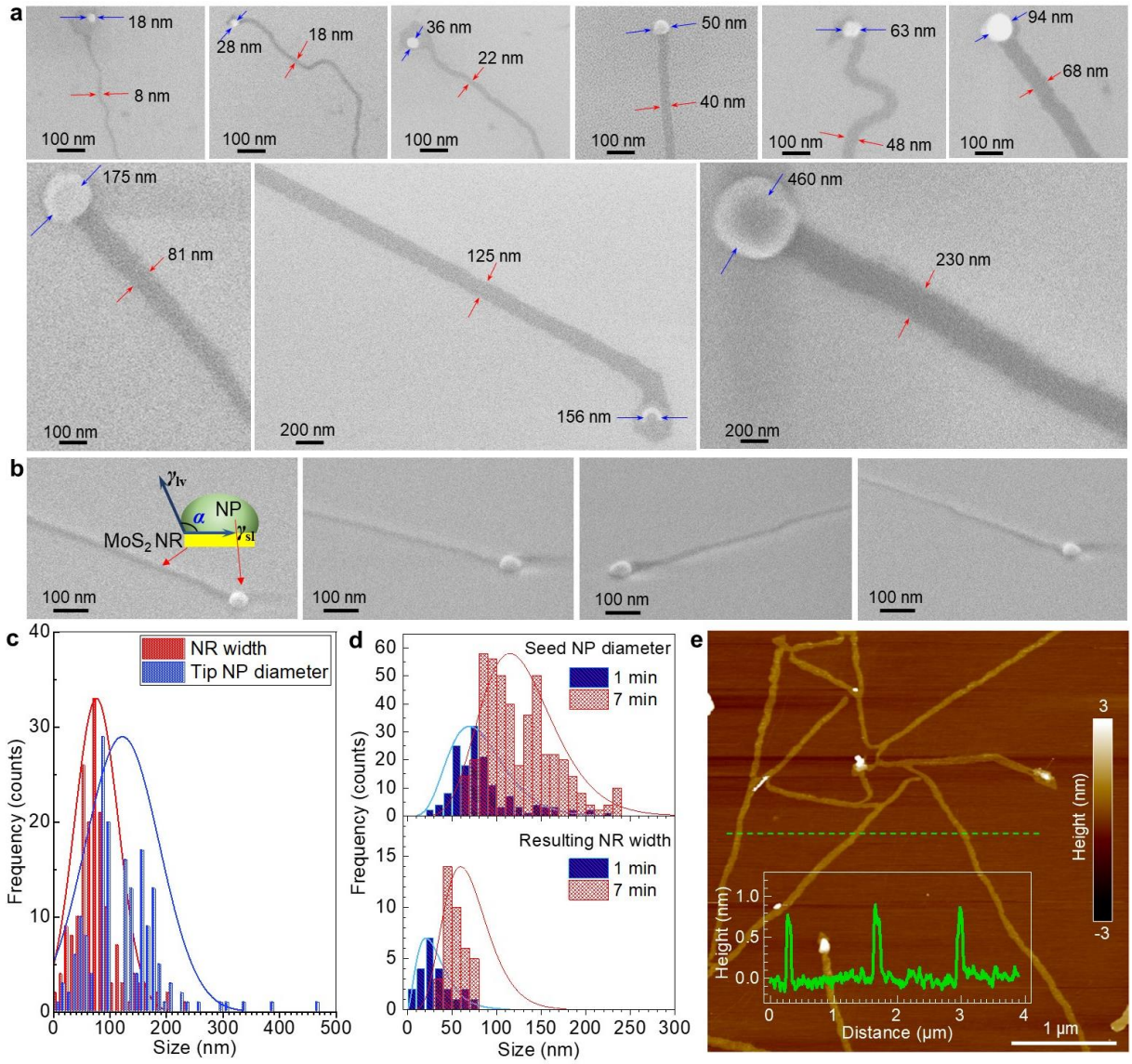

Supplementary Fig. 2. Characterization of SL MoS_2 NRs. (**a**) SEM images showing a series of grown MoS_2 NRs with different widths ranging from 8 to 230 nm and corresponding tip Ni NPs. The NP diameter is generally ≈1.2 to 2 times larger the NR width. (**b**) SEM images of NRs with tip NPs acquired by tilting the substrate to show wettability of the NP on the interface with corresponding NRs. Insert is the schematic illustration showing the front-view of NP-NR contact angle. (**c**) Distribution of NR widths and corresponding tip NP diameters (**d**) Diameter distribution of seed NPs deposited for 1 and 7 min (up) and width distribution of corresponding resulting NRs (down). (**e**) AFM image of SL MoS_2 NRs and height profile along the dashed line, confirming SL NR. The color scale in (e) is linear. Source data are provided as a Source Data file.

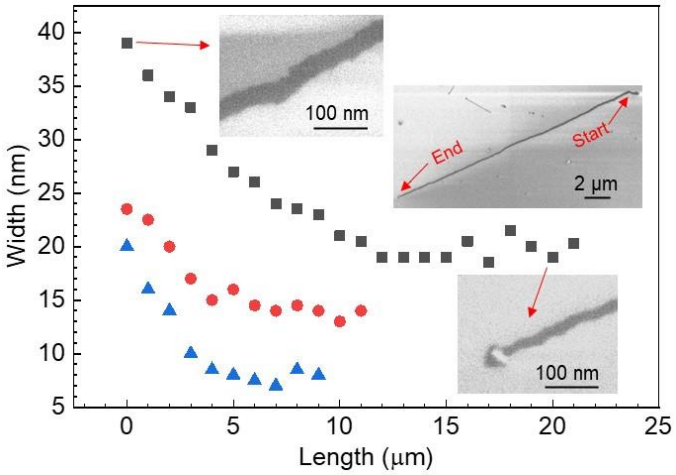

Supplementary Fig. 3. Three typical plots of width change along the length of an individual NR. Inset in the middle is a SEM image of the NR shown by black squares. The start side (upper inset SEM image) is wider than the end part (lower inset SEM image). The NR width reduces as the ribbon grows longer, then keeps approximately unchanged at some point till the end. The initial width is generally $\approx$2 times wider than the final width. Source data are provided as a Source Data file.

In our growth method, the seed droplet is the only source for Mo atoms, therefore NR growth inevitably leads to reduction of droplet size because of irreversible consumption of Mo atoms from the droplet by grown NR.

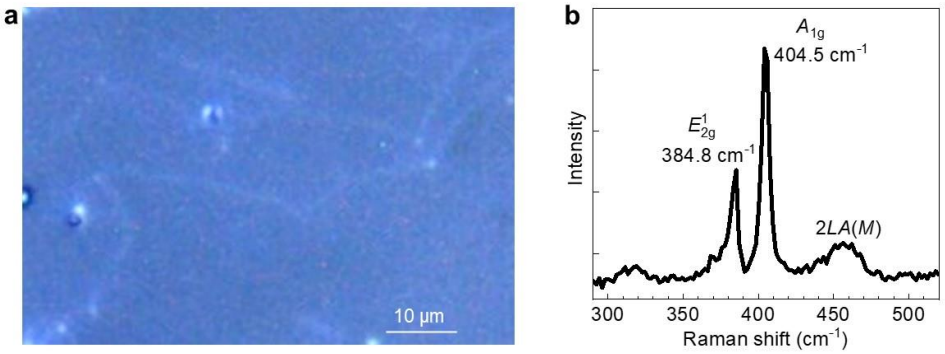

Supplementary Fig. 4. Raman spectrum of MoS_2 NRs grown on F-mica. (**a**) Optical microscope image of SL MoS_2 NRs grown on F-mica. (**b**) Raman spectrum of the MoS_2 NR shown in (a) excited by 532 nm laser, showing an energy difference of 19.7 cm^{-1} between A_{1g} and $E^1{}_{2g}$ mode, characteristic of SL MoS_2. Source data are provided as a Source Data file.

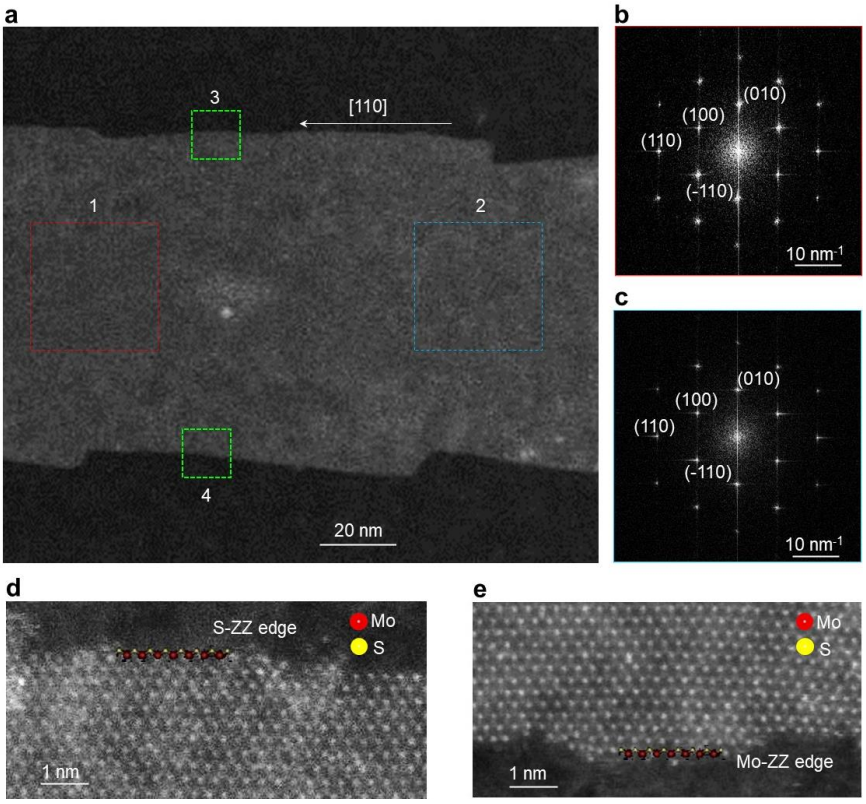

Supplementary Fig. 5. STEM characterization. (**a**) Low-magnification STEM image of a SL MoS_2 NR. (**b**, **c**) FFT patterns acquired from region 1 and 2 indicated by the dashed red and blue boxes, respectively, in (a), indicating the growth axis of this NR along the [110] crystal direction. The good alignment between the NR and diffraction pattern orientation indicates the NR is single crystal. (**d**, **e**) Atomic-resolution HAADF-STEM images acquired from region 3 and 4, respectively, as indicated by corresponding green dashed boxes in (a), showing that one side of the NR has a S-terminated zigzag (S-ZZ) edge (i.e., dashed green box 3), while the other side has a Mo-terminated zigzag (Mo-ZZ) edge (i.e., dashed green box 4).

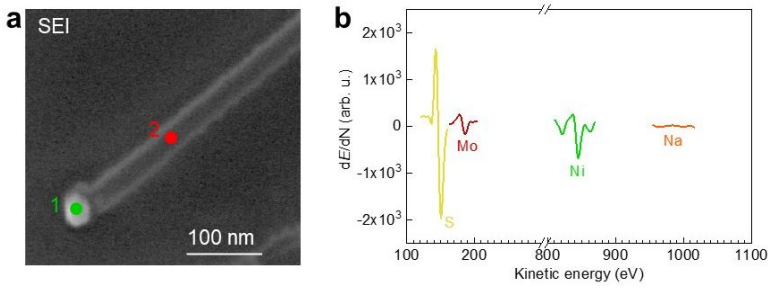

Supplementary Fig. 6. AES measurement of the SL MoS_2 NR. (**a**) Secondary electron image of the NR as shown in Fig. 2a. (**b**) AES spectra of Mo (red), S (yellow), Na (orange), and Ni (green). The signal of Ni was collected from spot 1, while Mo, S, and Na were collected from spot 2 in (a). Source data are provided as a Source Data file.

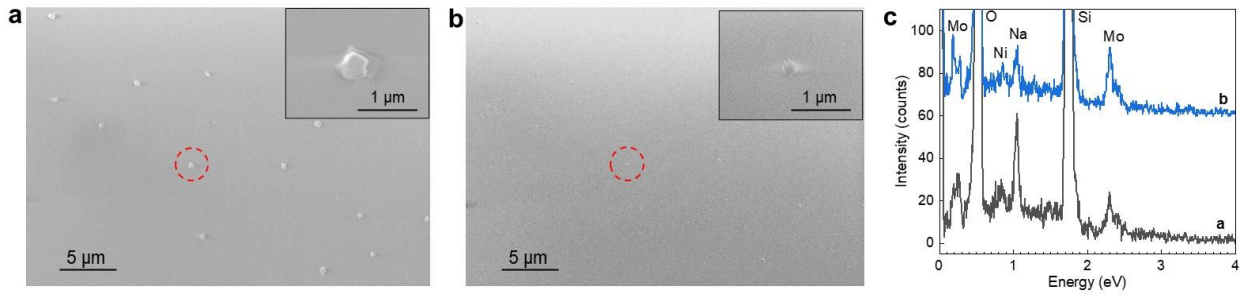

Supplementary Fig. 7. SEM characterizations of seed NPs. (**a**) SEM image of seed NPs deposited in step 1. (**b**) SEM image showing the same area as in (a) after annealing at 750 ºC for 1 minute under Ar flow. Insets are enlarged views of the circled NPs in (a) and (b). (**c**) EDS spectra of the NPs circled in (a) and (b). Source data are provided as a Source Data file.

It is clear that without sulfur, after annealing the NPs did not move and there is no precipitation out of the NPs. The NP sizes are reduced due to evaporation during the annealing. The overall composition does not change after annealing. These experimental results confirm that without sulfur, there is no precipitation and no moving of the droplets, even though they are liquified at the annealing temperature, proving the sulfur is the reason for precipitation and therefore moving of the NP.

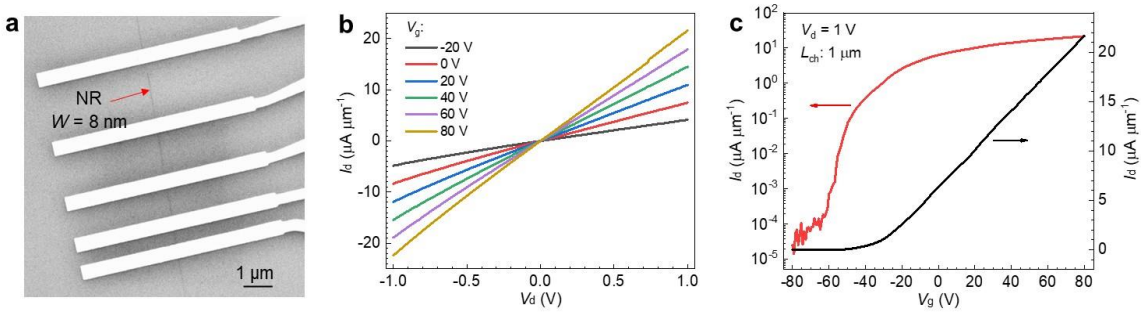

Supplementary Fig. 8. Electrical properties of SL MoS_2 NR. (**a**) SEM image showing a back-gate field-effect transistor (FET) made on an 8 nm width SL MoS_2 NR transferred on a SiO_2/Si^{++} substrate with Bi deposited as source-drain contacts. Bi was used as contacts due to low contact resistance with MoS_2 (ref.[1]). (**b**) Output (I_d-V_d) curves at different back-gate voltage (V_g) measured from a channel length (L_{ch}): 1 μm. The linear curves indicate good contacts. (**c**) Transfer curves (I_d-V_g, in both linear and logarithm scale). The MoS_2 NR shows a typical n-type behavior with an on/off ratio of $\approx 10^6$, and a current density up to 22 μA μm^{-1} within the applied V_g range. Source data are provided as a Source Data file.

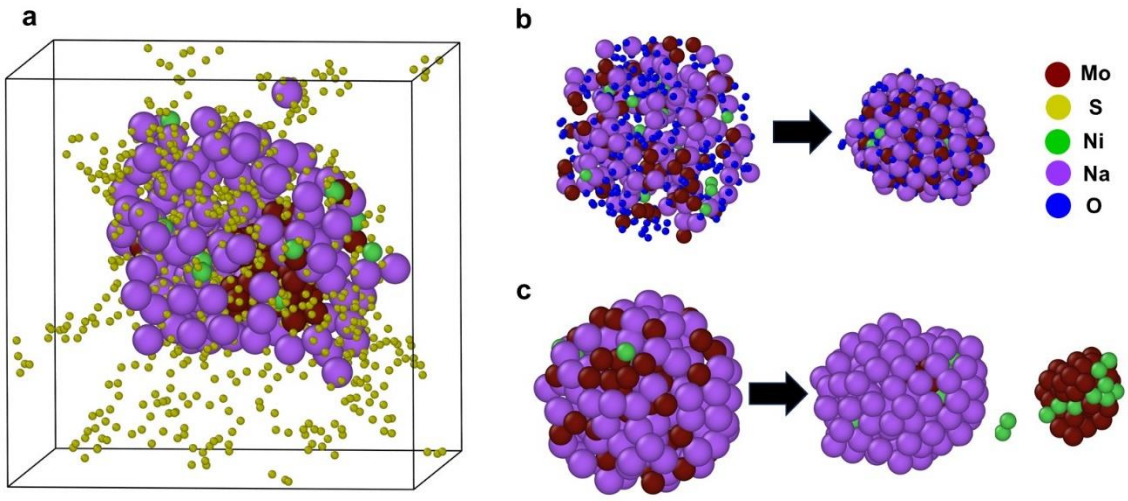

Supplementary Fig. 9. MD simulation. (**a**) A Na-Mo-Ni nanoparticle (without oxygen) interactions with S atoms, showing that it basically keeps a core-shell structure but with some Ni atoms on surface after the entire system being equilibrated at 650 K for 5 ns. (**b**, **c**) Oxygen effects on element distributions in nanoparticles. (b) nanoparticle with a high concentration of oxygen atoms leads to relatively uniform distribution of various elements after equilibration at 650 K for 1 ns; (c) nanoparticle without oxygen atoms leads to elements segregations after equilibrated at 300 K for 1 ns: Mo and Ni are mixed in the interior of nanoparticle while Na atoms are separated onto the surface of nanoparticle.

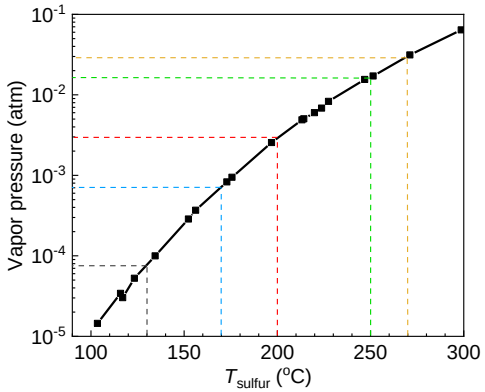

Supplementary Fig. 10. Sulfur vapor pressure (P_{sulfur}) dependence on the temperature (T_{sulfur}). Source data are provided as a Source Data file.

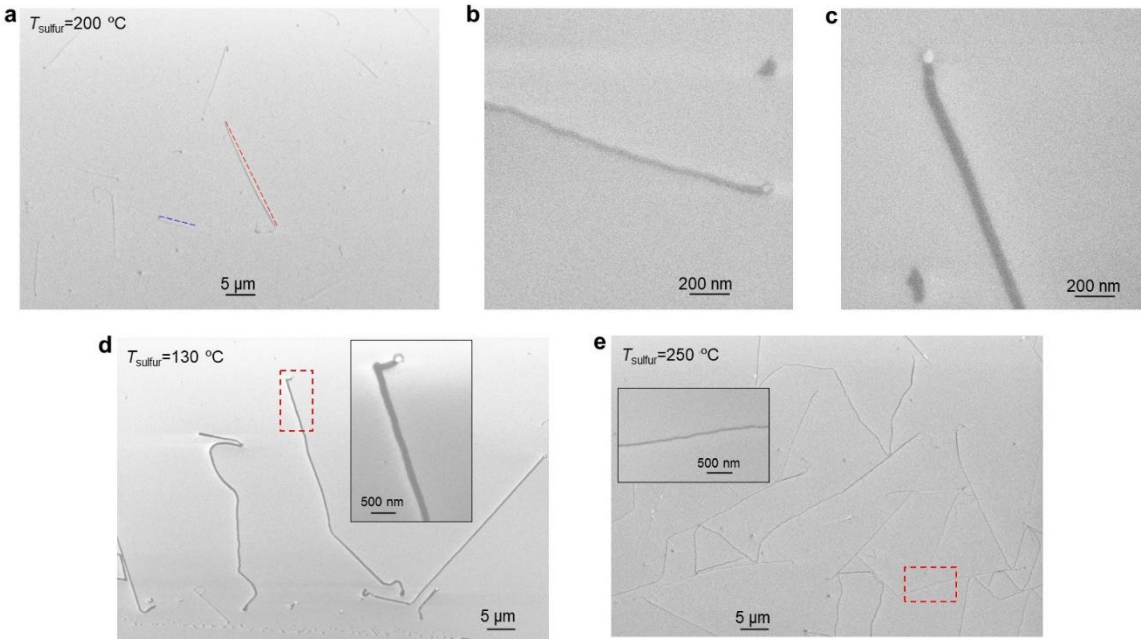

Supplementary Fig. 11. SEM images for NR length (*L*) *vs.* width (*W*) study. (**a**) A typical SEM image of SL MoS_2 NRs grown at 730 ºC for 180 s with the heating temperature for sulfur powder (T_{sulfur}) at 200 ºC. Dashed lines indicate a longer NR (red) and a shorter NR (blue). (**b**, **c**) Enlarged view of the longer, wider NR and the shorter, narrower NR indicated in (a). (**d**, **e**) SEM image of SL MoS_2 NRs grown at 730 ºC for 180 s with T_{sulfur} = 130 and 250 ºC, respectively. Insets are enlarged views of the red-boxed areas.

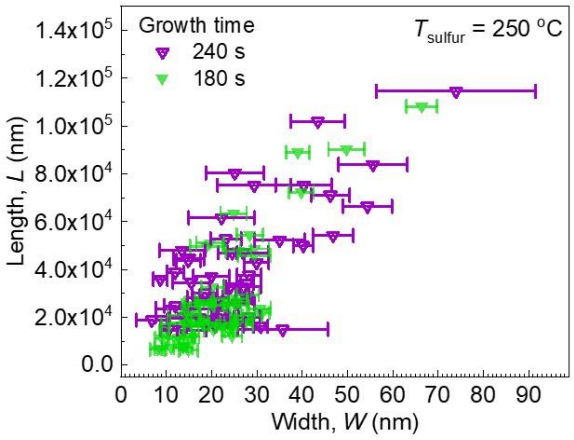

Supplementary Fig. 12. NR *L vs. W* relation. Statistics on dependence of MoS_2 NR *L* on *W* after sulfurization at 730 ºC with T_{sulfur} at 250 ºC for 180 s (green symbols) and 240 s (purple symbols) for comparison. The *L* vs *W* data of the NRs have been collected from three independent growth experiments at a given growth temperature (730 ºC) and T_{sulfur} at 250 ºC for each growth time. The error bars represent the variations of width along the length of each NRs. The NRs are generally longer after growth for 240 s than those for 180 s. Source data are provided as a Source Data file.

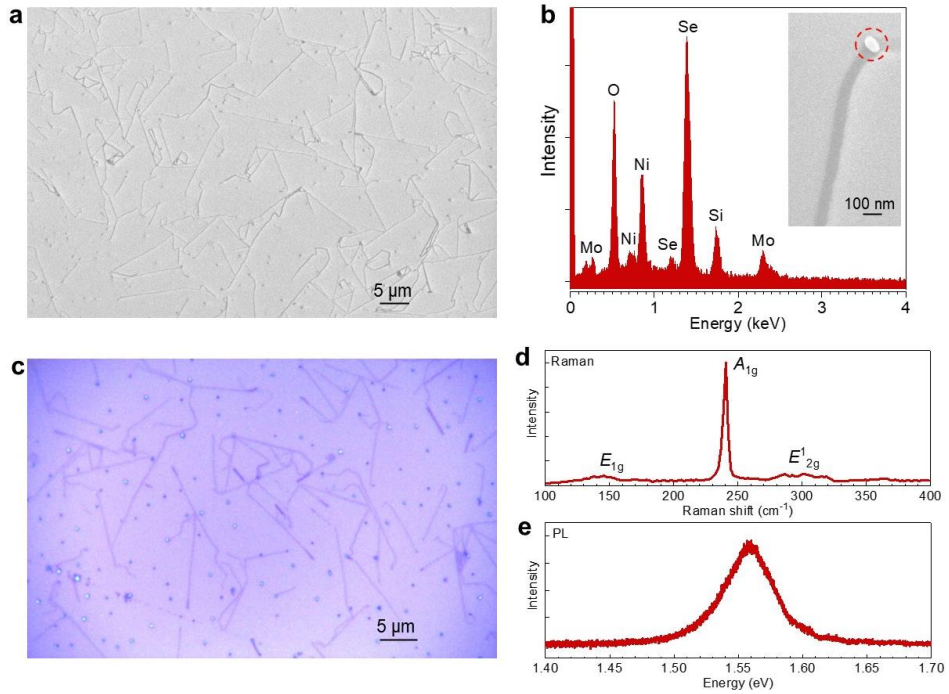

Supplementary Fig. 13. Growth of SL $MoSe_2$ NRs. (**a**) SEM image of SL $MoSe_2$ NRs grown from pre-deposited Na-Mo-Ni-O seed NPs on F-mica. The grown NRs were transferred onto a SiO_2/Si substrate for elemental analysis and optical measurement. (**b**) EDS spectrum of the tip NP on the grown $MoSe_2$ NR (inset) transferred on a SiO_2/Si substrate. (**c**) Optical microscope image of SL $MoSe_2$ NRs transferred on a SiO_2/Si substrate. (**d**) Typical Raman and (**e**) PL spectra of SL $MoSe_2$ NRs measured from those in (c). Source data are provided as a Source Data file.

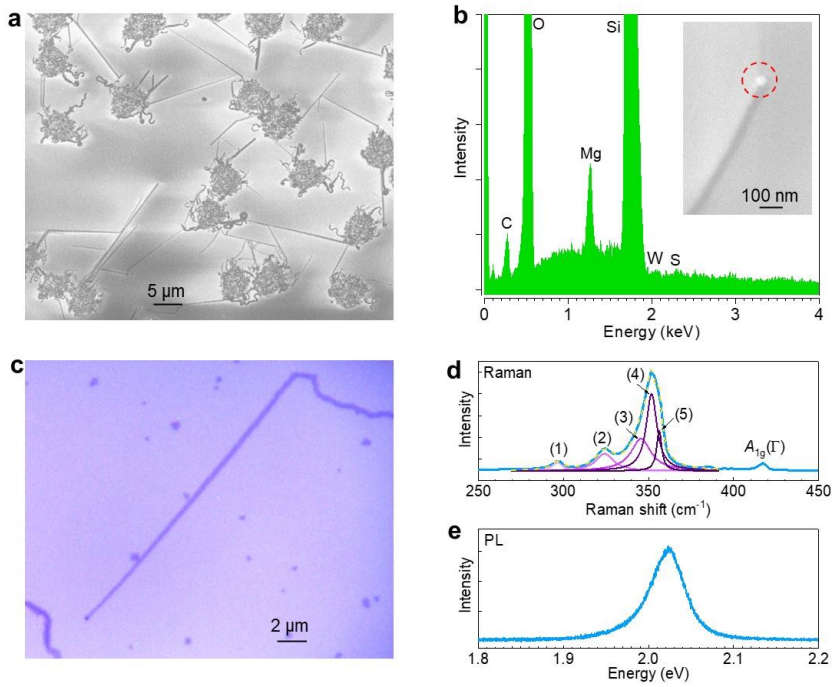

Supplementary Fig. 14. Growth of SL WS_2 NRs. (**a**) SEM image of SL $MoSe_2$ NRs grown from pre-deposited Na-W-Mg-O seed NPs on F-mica. The grown NRs were transferred onto a SiO_2/Si substrate for elemental analysis and optical measurement. (**b**) EDS spectrum of the tip NP on the grown WS_2 NR transferred on a SiO_2/Si substrate. (**c**) Optical microscope image of a SL WS_2 NR transferred on a SiO_2/Si substrate. (**d**) Typical Raman and (**e**) PL spectra of SL WS_2 NRs measured from that in (c). The vibration mode in the Raman spectrum labeled as (1) to (5) correspond to $2LA(M)$-$2E^2_{2g}(\Gamma)$, $2LA(M)$-$E^2_{2g}(\Gamma)$, $E^1_{2g}(M)$, $2LA(M)$, and $E^1_{2g}(\Gamma)$, respectively. Source data are provided as a Source Data file.

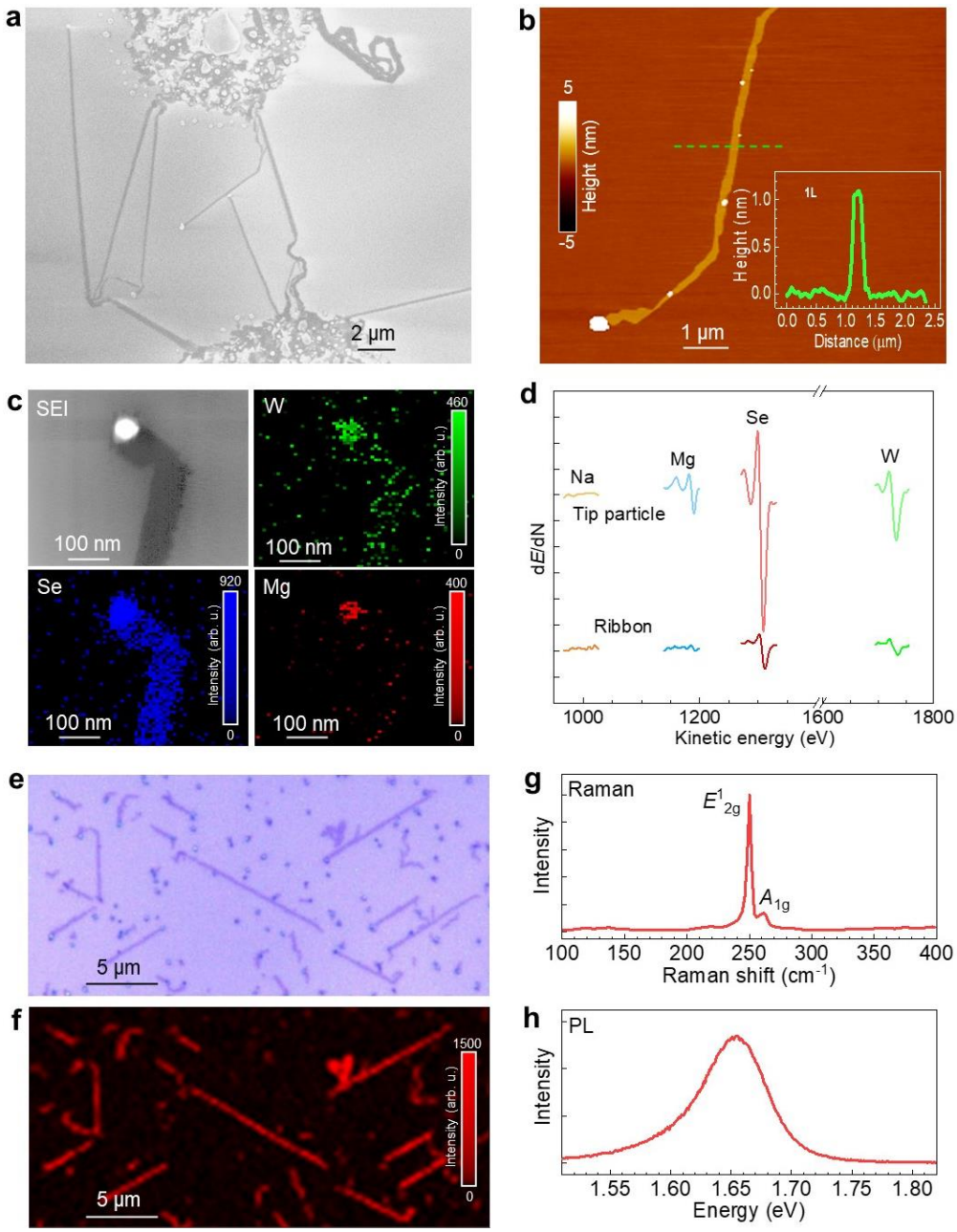

Supplementary Fig. 15 Growth of SL WSe_2 NR. (**a**) SEM image of WSe_2 NRs grown from pre-deposited Na-W-Mg-O seed particles on F-mica. (**b**) AFM image of a WSe_2 NR with the tip NP. Inset is the height profile along the dashed green line, indicating single layer. (**c**) AES elemental mapping of W, Se, and Mg of a SL WSe_2 NR including the tip NP. (**d**) AES spectra of the tip NP and the NR. For AES measurement, the NRs were transferred onto a SiO_2/Si substrate. (**e**) Optical microscope image of WSe_2 NRs transferred on a SiO_2/Si substrate. (**f**) Corresponding mapping on the integrated PL intensity of A-exciton emission band shown in (h). (**g**) Typical Raman and (**h**) PL spectra of SL WSe_2 NRs measured from those in (e). The color scales in (b), (c), and (f) are linear. Source data are provided as a Source Data file.

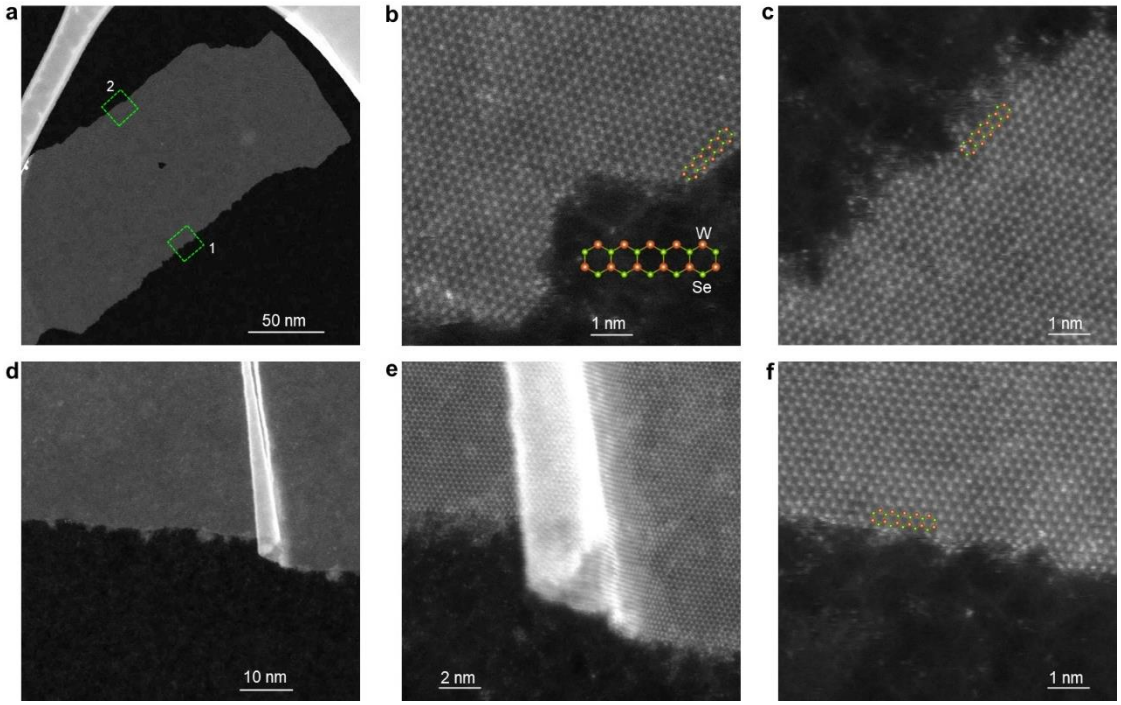

Supplementary Fig. 16. Atomic structure of SL WSe_2 NRs revealed from STEM characterization. (**a**) Low-magnification STEM image of a WSe_2 NR. (**b**, **c**) Atomic resolution HAADF-STEM images showing that one side of the NR has a W-terminated zigzag (W-ZZ) edge (i.e., dashed green box 1), while the other side has a Mo-terminated zigzag (Mo-ZZ) edge (i.e., dashed green box 2). (**d**) Low-magnification STEM image of a WSe_2 NR with a fold/ripplocation. (**e**, **f**) Atomic resolution HAADF-STEM images showing atomic structure around the fold (e) and the Se-ZZ edge (f).

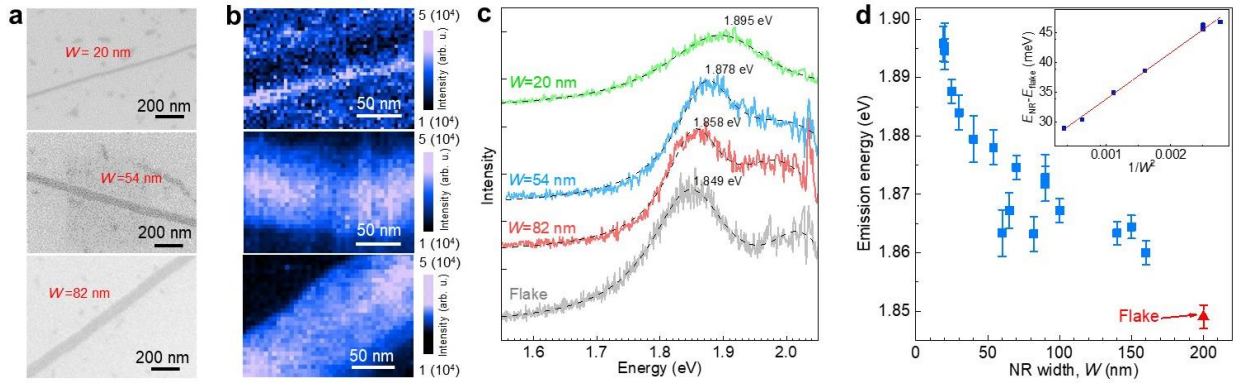

Supplementary Fig. 17. TEPL measurement on SL MoS_2 NRs at room temperature. (**a**) SEM images and (**b**) corresponding TEPL imaging of typical MoS_2 SL NRs with width (W) of 20 nm, 54 nm, and 82 nm. The color scales in (b) are linear. The measurements were conducted on NRs on SiO_2/Si substrate through a dry-transfer method. (**c**) Corresponding TEPL spectra of the NRs. The TEPL spectrum from a CVD-grown SL MoS_2 flake is also shown for comparison. The excitation is 594 nm. The spectra are offset for clarity. (**d**) Dependence of the A-exciton emission peak energy on the width of SL MoS_2 NRs. The emission energy of the SL flake is also indicated. Each point is the peak value of Gaussian fitting for corresponding TEPL spectra (as shown in (c)) measured from 17 different NRs with width from 20 to 160 nm. The error bars represent the deviation of Gaussian fitting for the peak. Inset is the dependence of the difference between emission energy of NR and flake (E_{NR}-E_{flake}) on $1/W^2$. Source data are provided as a Source Data file.

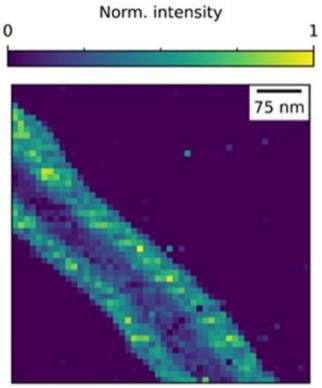

Supplementary Fig. 18. TEPL imaging of a nanoribbon with a width of ≈135 nm. Distinct edge regions are observed in the nanoribbon which may influence the width-dependent PL observed. The color scale is linear.

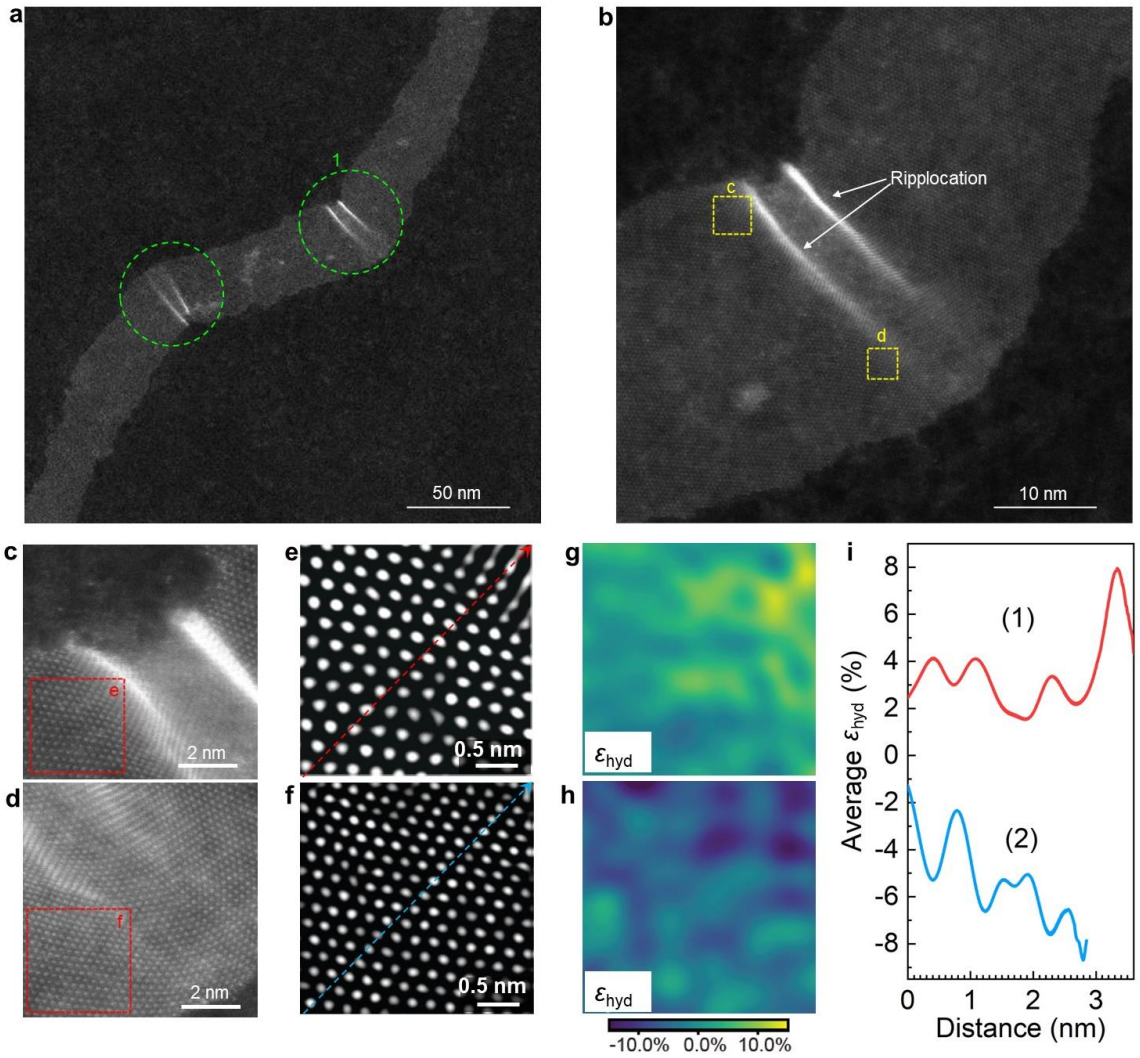

Supplementary Fig. 19. Atomic-resolution characterization of elastic strain in a MoS_2 NR. (**a**) Low-magnification HAADF-STEM image highlighting a MoS_2 NR with kinks, as indicated by dashed circles. This NR is the one as shown in Fig. 1f. (**b**) Enlarged view of the region included in the dashed green circle 1 in (a). Two ripplocations in the NR are indicated. (**c**, **d**) Atomic-resolution HAADF-STEM images of the regions contained by corresponding dashed yellow boxes in (b). (**e**, **f**) Filtered atomic-resolution HAADF-STEM images for dashed red box e and f in (c) and (d), respectively. (**g**, **h**) In-plane hydrostatic strain mapping of (e) and (f), respectively. The local elastic strain ranges from -14% to 14%. The color scale in (h) is linear. This elastic strain approached the theoretical limit of elastic strain in MoS_2 (ref.[2]), suggesting a significant potential for deep elastic strain engineering. (**i**) Variation of the in-plane hydrostatic strain along the red dashed line in (e) (red curve) and blue dashed line in (f) (blue curve), revealing a higher magnitude of strain in proximity to the ripplocation.

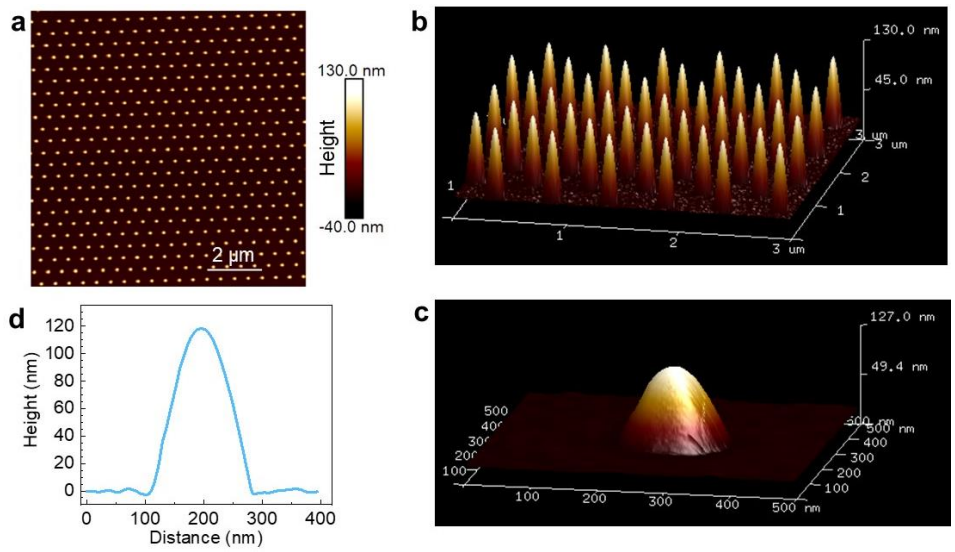

Supplementary Fig. 20. AFM characterization on Au nanocones. (**a**) AFM image of array of Au nanocones fabricated on a SiO_2/Si substrate. The color scale in (a) is linear. (**b**, **c**) 3D vision of AFM images of array and individual Au nanocone. (**d**) Hight profile of the Au nanocone shown in (c), through the apex.

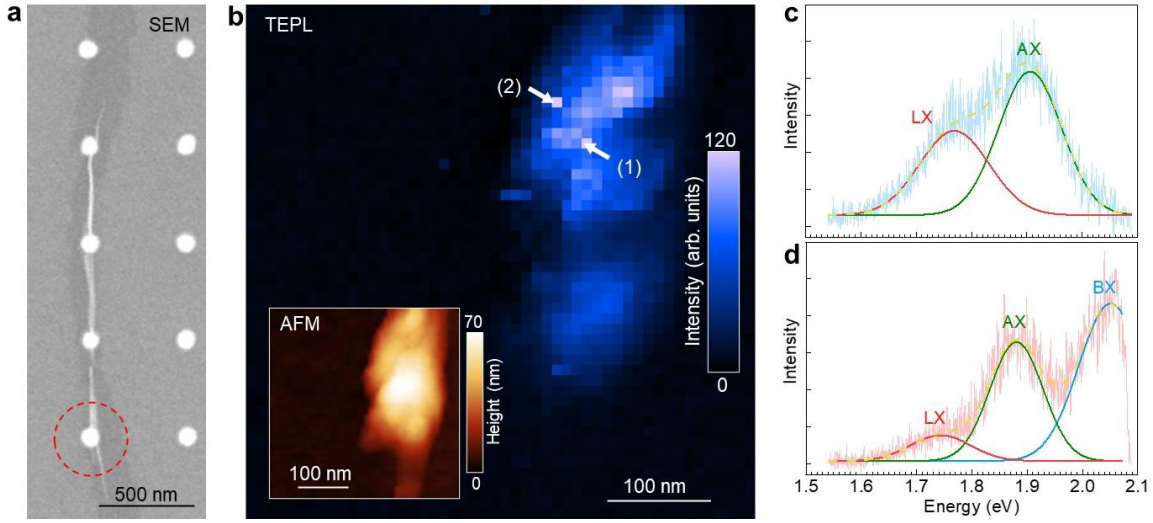

Supplementary Fig. 21. Visualization of hyperlocalized NR emissive states formed on the gold nanocones. (**a**) SEM image of a SL-MoS_2 NR on gold nanocones. (**b**) Nearfield TEPL imaging of the ROI indicated in panel (a) of the locally strained SL MoS_2 NR. The color scales in (b) are linear. (**c**, **d**) TEPL spectra extracted from the point (1) and (2) indicated in (b), indicating that the localized emission is composed of the A exciton (AX) band as well as a low-energy localized exciton (LX) emission band. Source data are provided as a Source Data file.

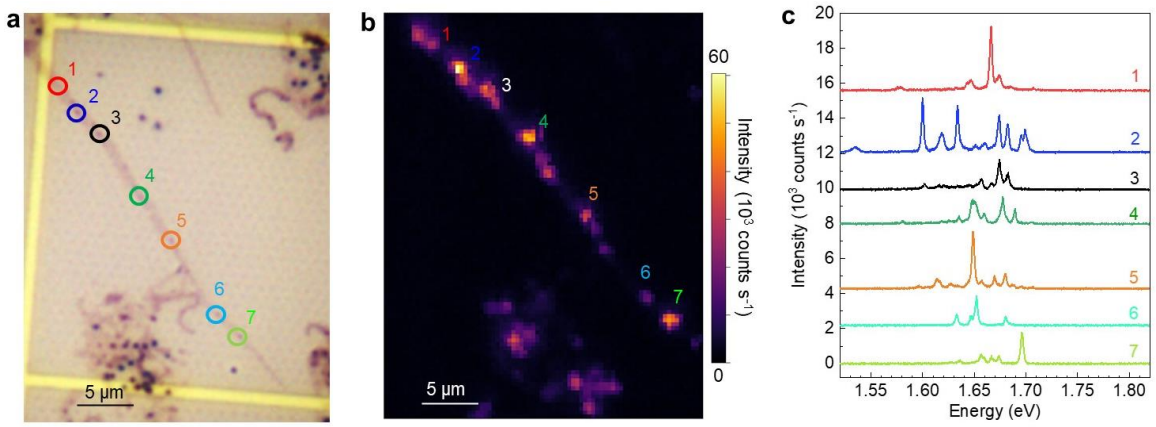

Supplementary Fig. 22. Deterministic quantum light emission from strained SL WSe_2 NR. (**a**) Optical microscope image of a SL WSe_2 NR transferred on an array of Au nanocones (the same NR as shown in Fig. 4c). (**b**) Map of integrated PL (at 4 K) intensity from the WSe_2 NR shown in (a). The emitters indicated by colored numbers correspond to the color circled spots in (a). The color scale in (b) is linear. (**c**) PL spectra of each emitter indicated in (b). Quantum emission appears at each site where the NR is draped over the cones, giving deterministic quantum emission. Source data are provided as a Source Data file.

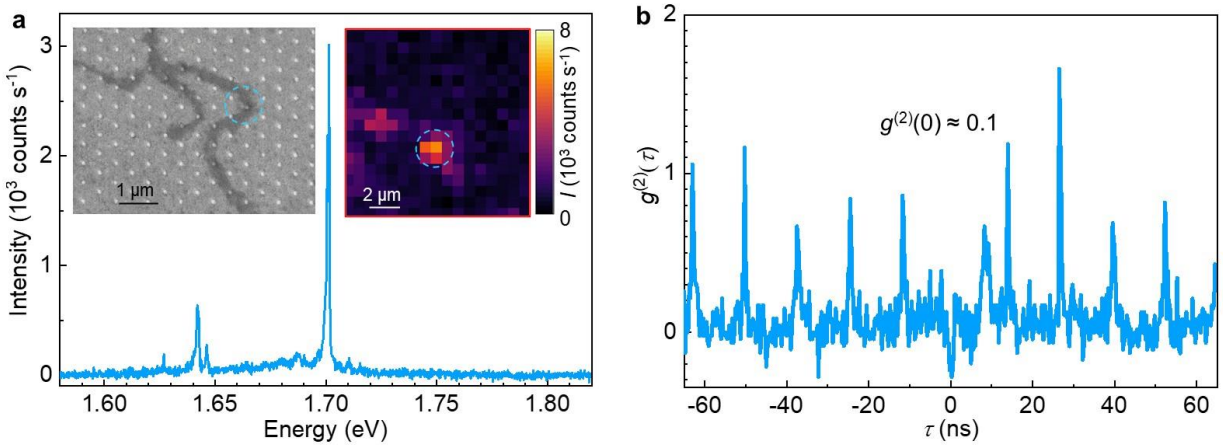

Supplementary Fig. 23. Quantum light emission from strained SL WSe_2 NR. (**a**) PL spectra of another strained SL WSe_2 NR by Au nanocone. Inset: SEM image of SL WSe_2 NRs transferred on an array of Au nanocones (left) and map of integrated PL intensity from the WSe_2 NR sample near the emitter indicated by the dashed blue circle (right). The color scale in (a) is linear. (**b**) $g^{(2)}(\tau)$ measurement of the emitter at 1.70 eV using pulsed excitation (rep. rate: 78 MHz). Because the measurement uses pulsed excitation, a peak at every τ = 12.8 ns is shown. The absence of the peak at a time delay of τ = 0 ns indicates that the emitter is anti-bunched with a single photon purity of 89%. The broad peak at τ =10 ns is the afterglow from APD. Source data are provided as a Source Data file.

Supplementary Notes

Suppl. Note 1. Controlling the width-distribution of NRs.

As shown in Fig. 3b, higher sulfur vapor pressure activates catalytic nanoparticles with smaller diameters, which leads to the growth of NRs with narrower width distribution. This is related to the fact that the pre-deposited nanoparticles always have a finite size distribution. However, further reduction of nanoparticles size is limited by the formation of proper composition of quaternary nanoalloy and further increasing sulfur vapor pressure can disturb the reactions. Therefore, there always will be some width distribution, yet it can be very narrow. For low or intermediate sulfur pressures there always will be broader width distribution, since it will activate nanoparticles with broader size distribution, unless catalyst particles (properly alloyed) could be created for given diameters with very narrow distribution. In addition to the sulfur vapor pressure, we also investigated an alternative approach, i.e., effect of growth temperature on the width distribution of the grown NRs. Specifically, we exploited the diameter-dependent melting temperature of NPs given that NR growth follows the VLS mechanism. Lowering the synthesis temperature can selectively activate (liquify) only smaller NPs, thereby favoring the growth of narrower NRs. As shown in the histograms below, lower growth temperatures in combination with experimentally possible highest sulfur vapor pressure result in growth of narrower NRs with narrower width distribution. Above all, while achieving selective growth of NRs with specific widths remains challenging, careful control over both sulfur vapor pressure and growth temperature enables the preferential growth of narrow NRs with a tight width distribution.

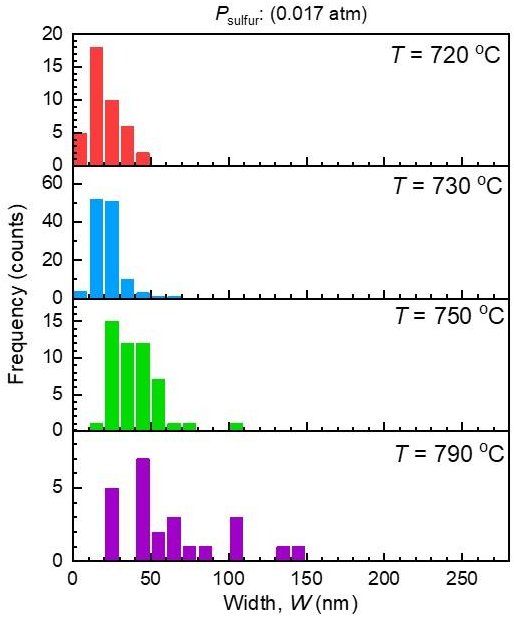

Supplementary Fig. 24. Width distribution of grown MoS_2 NRs with different growth temperatures under the same sulfur vapor pressure (P_{sulfur}: 0.017 atm, 250 °C heating temperature).

Suppl. Note 2. Parameters for calculations based on Gibbs-Thomson model.

$\Delta\mu_{vl}/(k_BT)$ is supersaturation of S atoms in the droplet with diameter (d), which equals to $\ln(P_{sulfur}/P_d)$, in which P_{sulfur} is the sulfur vapor pressure in our growth chamber, determined by the heating temperature (T_{sulfur}) as shown in Supplementary Fig. 10, while P_d the elevated equilibrium pressure of S in the droplet. $\Delta\mu_\infty/(k_BT)$ is the supersaturation between S vapor and the droplet with infinite interface, which equals to $\ln(P_{sulfur}/P_d)$, in which P_∞ is the sulfur pressure on the infinite boundary of S and droplet. According to the Gibbs-Thomson model,

$$\Delta\mu_{vl}/(k_BT) = \Delta\mu_\infty/(k_BT) - 2\sigma_{vl}\Omega/(dk_BT) \quad (1)$$

$$V_g = K_g(\Delta\mu_{vl}/(k_BT))^n = K_g\,(\Delta\mu_\infty/(k_BT) - 2\sigma_{vl}\Omega/(dk_BT))^n \quad (2)$$

in which V_g is the NR growth rate, K_g is the kinetic factor, and n is the order (in our case, n = 1 or 2). σ_{vl} is the surface energy of Ni-Mo alloy ($\approx$1.7 J m^{-2}), Ω is the S atomic volume in the droplet (0.0056 nm^3), $k_B = 1.380649 \times 10^{-23}$ J K^{-1}, and T = 1003 K is the synthesis temperature. The droplet diameter d is correlated with NR width W: $d \approx W/0.75$. Using the above equation, we fit the experimental data of V_g vs $1/W$ (Fig. 3c) for each P_{sulfur} with n = 1, from which the critical values could be extracted from the interceptions of the fitting lines with the $1/W$-axis: $\Delta\mu_\infty(P_{sulfur})/(k_BT) = 1.33\sigma_{vl}\Omega/(W_c k_BT)$, as shown in Table 1.

It should be noted that for the choice surface energy value of the droplet, as there is no data on the quaternary phase diagram or surface energy of molten Na-Mo-Ni-O nanoalloy, we use the most reasonable available data from literature. The surface energy of pure Ni is $\approx$1.653–1.863 J m^{-2}, and Ni-Mo droplet has a close surface energy about 1.6–1.8 J m^{-2}. According to our experimental results, a pure Ni NP is attached to the NR tip after growth ending. Taking into account that the molten pure Ni and Ni-Mo has close surface tension values and Mo is one of the elements to precipitate for the formation of NR, we thereby use the surface energy value of Ni-Mo alloy for our calculations.

Suppl. Note 3. Quantum emission from strained SL MoS_2 NR

Although localized strain-induced bright narrowband emissions from QD-like states in SL flakes of WSe_2, WS_2, and $MoSe_2$ at cryogenic temperatures are firmly established by many experimental studies[3-6], observations of analogous emitters in SL MoS_2 are mostly lacking. So far fewer experimental reports of quantum light emission in SL MoS_2 have relied on the deliberate and precise generation of localized defects with a He ion focused ion beam (FIB)[7]. The strain-induced quantum light emission from SL MoS_2 is for the first time reported in this work. Possible mechanisms revealed in theoretical studies include strain-induced confinement due to nano-wrinkles[8,9] and hybridization of band-edge defect states with excitons where the energy of the exciton is reduced to that of the defect level by the localized strain[10]. We speculate that in the SL MoS_2 NR here, sufficient localized strain is achieved to realize optically active, strain-induced QD-like states. The localization may be enhanced by the nanoribbon geometry, and we do not observe any signatures of the hybridization with defect states (such as significant line narrowing).

Supplementary references

1. Shen, P. -C. *et al*. Ultralow contact resistance between semimetal and monolayer semiconductors. *Nature* **593**, 211–217 (2021).
2. Han, Y. *et al.*, Deep elastic strain engineering of 2D materials and their twisted bilayers. *ACS Appl. Mater. Interfaces* **14**, 8655–8663 (2022).
3. Palacios-Berraquero, C. *et al.* Large-scale quantum-emitter arrays in atomically thin semiconductors. *Nat. Commun.* **8**, 15093 (2017).
4. Micevic, A. *et al.* On-demand generation of optically active defects in monolayer WS_2 by a focused helium ion beam. *Appl. Phys. Lett.* **121**, 183101 (2022).
5. He, Y. M. *et al.* Single quantum emitters in monolayer semiconductors. *Nat. Nanotechnol.* **10**, 497–502 (2015).
6. Yu, L. *et al.* Site-controlled quantum emitters in monolayer $MoSe_2$. *Nano Lett.* **21**, 2376–2381 (2021).
7. Klein, J. *et al.* Site-selectively generated photon emitters in monolayer MoS_2 via local helium ion irradiation. *Nat. Commun.* **10**, 2755 (2019).
8. Carmesin, C. *et al.* Quantum-dot-like states in molybdenum disulfide nanostructures due to the interplay of local surface wrinkling, strain, and dielectric confinement. *Nano Lett.* **19**, 3182–3186 (2019).
9. Darlington, T. P. *et al.* Imaging strain-localized excitons in nanoscale bubbles of monolayer WSe_2 at room temperature. *Nat. Nanotechnol.* **15**, 854-860 (2020).
10. Linhart, L. *et al.* Localized intervalley defect excitons as single-photon emitters in WSe_2. *Phys. Rev. Lett.* **123**, 146401 (2019).